

Uncertainties in supernova input rates drive qualitative differences in simulations of galaxy evolution

Benjamin W. Keller^{*} and J. M. Diederik Kruijssen

Astronomisches Rechen-Institut, Zentrum für Astronomie der Universität Heidelberg, Mönchhofstraße 12-14, D-69120 Heidelberg, Germany

23 March 2022

ABSTRACT

Feedback from core collapse supernovae (SNe), the final stage of evolution of massive stars, is a key element in galaxy formation theory. The energy budget of SN feedback, as well as the duration over which SNe occur, are constrained by stellar lifetime models and the minimum mass star that ends its life as a SN. Simplifying approximations for this SN rate are ubiquitous in simulation studies. We show here how the choice of SN budget and timings (t_0 for the delay between star formation and the first SN, τ_{SN} for the duration of SN injection, and the minimum SN progenitor mass) drive changes in the regulation of star formation and outflow launching. Extremely long delays for instantaneous injection of SN energy ($t_0 \gg 20 \text{ Myr}$) reduces star formation and drive stronger outflows compared smaller delays. This effect is primarily driven by enhanced clustering of young stars. With continuous injection of energy, longer SN durations results in a larger fraction of SN energy deposited in low ambient gas densities, where cooling losses are lower. This is effect is particularly when driven by the choice of the minimum SN progenitor mass, which also sets the total SN energy budget. These underlying uncertainties mean that despite advances in the sub-grid modeling of SN feedback, serious difficulties in constraining the strength of SN feedback remain. We recommend future simulations use realistic SN injection durations, and bound their results using SN energy budgets and durations for minimum SN progenitors of $7 M_{\odot}$ and $9 M_{\odot}$.

Key words: galaxies : formation – galaxies : evolution – supernovae: general – galaxies : star formation – methods : numerical

1 INTRODUCTION

Supernovae (SNe) are important components of any theory of galaxy formation, in both (semi-)analytic models and hydrodynamic simulations. The energy and momentum injected by SNe stirs turbulence in the interstellar medium (ISM) (Joung & Mac Low 2006), drives the formation of a multiphase ISM (McKee & Ostriker 1977), and can launch galaxy-scale winds and outflows (Larson 1974). Modeling SNe in galaxy formation simulations has proven to be non-trivial. The failure of SNe to regulate star formation in early simulations (Katz 1992; Scannapieco et al. 2012) has led to significant effort to develop sub-grid treatments of SNe in simulations where the early, small-scale evolution of single SN remnants are unresolved (Thacker & Couchman 2000; Springel & Hernquist 2003; Stinson et al. 2006; Dalla Vecchia & Schaye 2012; Keller et al. 2014).

Any model for SN feedback must include choices for:

- The amount of energy/momentum injected (*the SN budget*).
- The timescale over which the injection occurs (*the SN rate*).

- A method to counteract numerical errors from the resolution of spatial/temporal discretization (*the sub-grid model*).

The most technically challenging of these is the final, and numerous studies have proposed different ways to properly treat the energy injected by feedback without dealing with “overcooling” and to achieve resolution convergence. Despite the great sophistication and success of many of these models, less consideration has gone into how the SN input rates and timescales change the impact of SN feedback on galaxy evolution. Instead, many have used very simplified assumptions about the SN budget and rate.

The “overcooling problem” was identified early on, in some of the first cosmological hydrodynamic simulations that included SN feedback (e.g. Katz 1992). In these simulations, SN energy was deposited into resolution elements that contained many orders of magnitude more mass than the SN ejecta. As such, two related problems arose. The first was that the Sedov radius for individual SNe was also many orders of magnitude smaller than the hydrodynamical resolution of the simulations. By failing to resolve the energy-conserving Sedov-Taylor phase (Taylor 1950), the amount of shock-heated gas becomes a function of numerical resolution alone. On top of this, the generation of momentum by this phase and the later pressure-driven snowplow (when the swept-up shell

^{*} Email: benjamin.keller ‘at’ uni-heidelberg.de

can cool, but the hot bubble remains adiabatic) is completely lost if the resolution isn't smaller than the Sedov radius (Sedov 1959). This minimum required resolution can be as small as ~ 1 pc in a typical galaxy (Hu 2019). The second problem, related to this, arises from the radiative cooling rate of the hot bubble. If too much mass is heated by SN feedback, the temperature of this bubble may be close to the peak of the radiative cooling curve at 10^5 K. If this occurs, the cooling time for the bubble will be artificially lowered, potentially by an order of magnitude or more (Dalla Vecchia & Schaye 2012). These two numerical effects can lead to SNe radiating nearly all of their energy away before they have a chance to either generate significant momentum or hot, buoyant gas that rises into the galactic halo (Keller et al. 2020). As the resolution required to avoid these problems is still beyond the reach of cosmological simulations, this has motivated the focus on numerical sub-grid models to overcome overcooling.

A great deal of work has been done to study the effects of changing the numerical method for coupling feedback energy and momentum to the ISM. Many new sub-grid feedback models that have been proposed in recent decades (e.g. Navarro & White 1993; Gerritsen 1997; Springel & Hernquist 2003; Scannapieco et al. 2006; Kimm & Cen 2014; Keller et al. 2014; Smith et al. 2018). As a result of this growing number of models, studies have been undertaken to try and quantify the effects of individual model parameters, as well as the differences between models. Two early attempts at this were Thacker & Couchman (2000) and Kay et al. (2002). Thacker & Couchman (2000) showed that in smoothed-particle hydrodynamics (SPH) simulations, the choice of how to smooth feedback energy over a region can have significant effects on whether feedback energy is lost to numerical overcooling. Kay et al. (2002) studied how kinetic feedback and thermal feedback implemented using the Gerritsen (1997) delayed cooling model varies in effectiveness for different cooling delay times and SN efficiencies. Unsurprisingly, they found lower star formation rates (SFRs) and cold gas fractions with higher feedback efficiencies. For thermal feedback with a cooling delay, they also found that star formation could be regulated only when unrealistically large delay times (approaching a Hubble time) were used. Subsequent studies have refined these results, as well as showing how many of the issues of numerical overcooling are alleviated through careful consideration of the unresolved evolution of feedback bubbles. Dalla Vecchia & Schaye (2012) showed that the amount of mass heated by feedback was a critical component to determining its effectiveness, while Kimm & Cen (2014) showed that attempting to match the terminal momentum of high-resolution studies of SN bubbles could produce a resolution-insensitive model for momentum injection via SN feedback.

The failure of the first generation of SN models also drove a push by simulators to examine additional forms of “early” (pre-SNe) feedback. Models have now been developed that include stellar winds, radiation pressure, and ionization by UV photons, in addition to SNe (e.g. Stinson et al. 2013; Agertz et al. 2013; Hopkins et al. 2014). Beyond the additional momentum and energy these mechanisms provide, they are believed to “prime” the regions of SN detonation, reducing the cooling losses experienced by SNe (Rogers & Pittard 2013). Beyond these more traditional forms of stellar feedback, significant work is now also being done to better understand the role of high-energy cosmic rays in heating and stirring the ISM (e.g. Jubelgas et al. 2008; Booth et al. 2013; Girichidis et al. 2016). Despite the complex array of potential sources of stellar feedback, there remains significant uncertainty in how SNe alone impact the evolution of galaxies.

A comprehensive comparison of simulations including different feedback, star formation, and hydrodynamic methods was undertaken by Scannapieco et al. (2012), who found that the choice of feedback model (as well as the underlying physical process driving that feedback) produces far greater variation in cosmological galaxy evolution than differences in hydrodynamics method. A more tightly controlled study by Rosdahl et al. (2017) implemented five different sub-grid models for feedback in the simulation code RAMSES (Teyssier 2002). These models were a simple thermal dump without any mechanism to control overcooling, a stochastic thermal model based on Dalla Vecchia & Schaye (2012); a delayed cooling model similar to Gerritsen (1997) first introduced in Teyssier et al. (2013); a kinetic feedback model introduced in Dubois & Teyssier (2008); and a mechanical feedback mechanism based on Kimm & Cen (2014). Using the same initial conditions, star formation method, and hydrodynamics solver allowed them to control their study to look at the impact of the feedback sub-grid model alone. They found significant differences in the qualitative appearance of their simulated galaxies, as well as quantitative changes in the star formation and outflow rates, outflow properties, and temperature-density phase diagrams.

The total energy budget and the duration of SN feedback for a stellar population depends both on stellar evolution and the initial mass function (IMF). Stellar evolution models can predict whether a star with a given mass and metallicity will end its life as a core-collapse SN (e.g. Smartt 2009), the energy released by that SN, and the lifetime of the star prior to SN detonation (e.g. Leitherer et al. 1999; Ekström et al. 2012; Leitherer et al. 2014). By calculating the range of stellar masses which produce SNe, we can use the IMF to determine the SN energy budget and rate of a stellar population. While there are constraints on many of these pieces, there are still sufficiently many uncertainties that the total amount of energy released by SNe cannot be well constrained with better than ~ 50 per cent uncertainty. Because the lowest mass SN progenitors have the longest lifetimes, this also leads to a corresponding uncertainty in the duration over which SN feedback occurs, τ_{SN} . This picture is complicated by the fact that many simulation approaches simply ignore the different lifetimes of stars, injecting an entire stellar population's SN budget instantaneously (e.g. Crain et al. 2015; Rosdahl et al. 2017). The total energy budget from one set of simulations to the next can vary by more than a factor of 2, and injection timescales can vary by tens of Myr (see Table 1).

The structure of this paper is as follows. First, we show how the SN injection rates and energy budget can be calculated, and compare this to a brief survey of injection rates used in the literature (Section 2). We then introduce a set of simulations of an isolated Milky Way galaxy analogue that we will use to study the effects of varying the SN injection rate and timescale (Section 3). With these simulations, we examine the impact of instantaneously injecting all SN energy after varying delay times (Section 4.1), comparing this to the effect of using a continuous injection based on the stellar lifetimes of SN progenitors (Section 4.2). We then show the importance of the minimum SN progenitor mass (Section 5). Finally, we conclude with a discussion of the implications of these results, and what is needed going forward to build simulations that offer strong predictive power (Section 6 and 7).

2 A SURVEY OF SUPERNOVAE INJECTION RATES

The starting point for determining the energy budget of SNe produced by a simple stellar population is the IMF (Salpeter 1955;

Simulations	$\mathcal{E}_{\text{SN}} (10^{49} \text{ erg}/M_{\odot})$	t_0 (Myr)	τ_{SN} (Myr)	SN Rate Form
Springel & Hernquist (2003)	0.400	0	0	Instantaneous
Dobbs et al. (2011)	0.625	0	0	Instantaneous
Dubois et al. (2012)	1.000	10	0	Instantaneous
Agertz et al. (2013)	1.014	4.92	35.21	Equation 5
Ceverino et al. (2014)	1.488	0	40	Constant Rate
EAGLE (Crain et al. 2015)	1.730	30	0	Instantaneous
AGORA Comparison (Kim et al. 2016)	1.080	5	0	Instantaneous
Snap, Crackle, Pop (Rosdahl et al. 2017)	2.000	5	0	Instantaneous
FIRE2 (Hopkins et al. 2018b)	1.060	3.4	34.13	Equation 6
MUGS2 (Keller et al. 2016)	1.010	4.92	35.21	Equation 5
Semenov et al. (2018)	1.000	0	40	Constant Rate
FOGGIE (Peeples et al. 2019)	1.787	$12t_{\text{dyn}}$	0	Instantaneous

Table 1. SN energy injection parameters for a set of simulations from the literature. We show here the total specific energy injected through SNe (\mathcal{E}_{SN}), the delay between star formation and the first SN event (t_0), and timescale over which SNe occur (τ_{SN}). As is clear, there is a spread in the total energy injected more than a factor of two, as well as a great variety in the SN delays and timescales. Many simulations deposit SN energy as a single event, sometimes at the time of the first SN, sometimes at the midpoint of the distribution, or sometimes at time of the final SN.

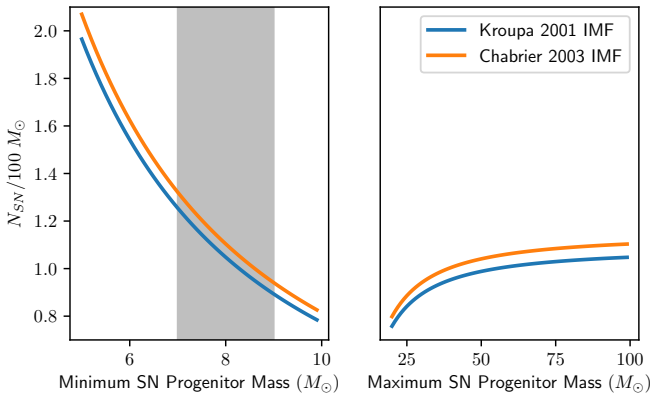


Figure 1. Variation in the number of SNe (N_{SN}) occurring for a stellar population for different minimum and maximum progenitor masses. The left panel show the change in N_{SN} for varying minimum mass with a maximum mass of $100 M_{\odot}$, while the right panel show the change with a minimum mass of $8 M_{\odot}$ and a varying maximum mass. Blue curves use a Kroupa (2001) IMF, while the orange curves use a Chabrier (2003) IMF. The vertical grey bar shows the best estimate minimum progenitor mass of $8 \pm 1 M_{\odot}$ (Smartt 2009). The maximum progenitor mass is much more uncertain, and may span the entire range shown here. As is clear, the minimum progenitor mass has a more significant impact on the SN budget than the choice of maximum progenitor.

Bastian et al. 2010; Offner et al. 2014). The typical form of the IMF is given as the number of stars in a logarithmic mass interval $\Phi(M) = dN/d \log M$. For high-mass stars, this is typically a power law $\Phi(M) = AM^{-\Gamma}$, with the ‘‘Salpeter slope’’ being $\Gamma \sim 1.35$. Naturally, the linear form of the IMF is related to the logarithmic form as $\mathcal{X}(M) = dN/dM = \Phi(M)/(M \ln 10)$. Taking the first moment of this IMF form allows us to determine the normalization for the IMF, such that the total mass integrates to unity. Unfortunately, if the IMF is a power-law, with a low-end slope $\Gamma > 1$, it will diverge for the lower limits of integration as $\lim_{M \rightarrow 0}$. This, along with better observations of low-mass stars, has led to the development of newer IMF forms, consisting of multiple power law IMFs, such as the commonly used Kroupa (2001)

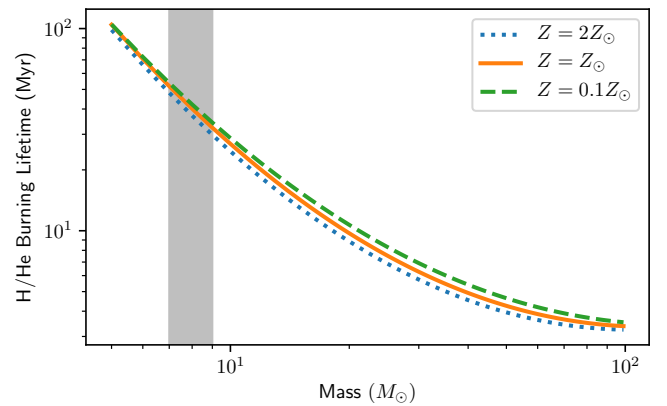


Figure 2. Hydrogen and Helium burning lifetimes as a function of stellar mass for stars with twice solar metallicity (blue dotted curve), solar metallicity (orange solid curve), and tenth solar metallicity (green dashed curve). The vertical grey bar shows the best-estimate minimum progenitor mass for SNe ($8 \pm 1 M_{\odot}$). As is clear, the mass of the star is a much stronger determinant for its lifetime than the star’s metallicity.

IMF:

$$\Phi(M) = A_k \begin{cases} 25M^{0.7} & 0.01 \leq M/M_{\odot} < 0.08 \\ 2M^{-0.3} & 0.08 \leq M/M_{\odot} < 0.50 \\ M^{-1.3} & 0.50 \leq M/M_{\odot} < 100 \end{cases} \quad (1)$$

An alternative form is to use a log-normal distribution with a power law tail, as in the (also common) Chabrier (2003) IMF.

$$\Phi(M) = A_c \begin{cases} 0.158 \exp\left(-\frac{(\log(M)+1.102)^2}{0.952}\right) & M/M_{\odot} \leq 1.0 \\ 0.28M^{-1.3} & M/M_{\odot} > 1.0 \end{cases} \quad (2)$$

With these forms, the lower mass limits no longer produce a divergent number of low-mass stars. None the less, we still wish to impose a lower limit on the mass of stars for physical reasons, as we expect there to be a minimum mass for core fusion in stars. We also expect there to be an upper mass limit, somewhere near the Eddington limit during the formation of massive stars. These mass limits are of course a matter of some debate, and can produce a

small change in the normalization of the IMF (A), on the order of 5 per cent for the most extreme variations in both the lower and upper integration limits. For this paper, we will use a lower limit of $0.01 M_{\odot}$ and an upper limit of $100 M_{\odot}$ for calculations involving the IMF. The normalization can be determined such that that $\Phi(M)$ is given per unit mass by solving:

$$\int_{0.01}^{100} M \mathcal{X}(M) dM = \int_{0.01}^{100} \frac{\Phi(M)}{\ln 10} dM = 1 \quad (3)$$

Together, this gives us a normalization for a [Kroupa \(2001\)](#) IMF of $A_k = 0.487$ and for a [Chabrier IMF](#) $A_c = 0.512$. The number of SNe that then occur for a population is simply $\int \mathcal{X} M dM$ integrated over the initial mass range of SN progenitors.

Determining the number of SNe that occur per unit mass of stars formed is then simply a question of choosing what masses of stars end their lives as a SN. The choice of these limits is critical, as is shown in [Figure 1](#). While the upper limit has less impact on the SN budget (because of the steep Salpeter slope at high mass), changing the minimum progenitor mass from $10 M_{\odot}$ to $6 M_{\odot}$ can change the total number of SNe occurring per unit mass by a factor of ~ 2 , doubling the energy budget for SNe. Converting the IMF into an SN rate is simply a question of combining it with a model for stellar lifetimes (as a function of their mass). [Raiteri et al. \(1996\)](#) has produced a fit for the Hydrogen and Helium burning lifetimes of stars computed by the Padova group ([Alongi et al. 1993](#); [Bressan et al. 1993](#); [Bertelli et al. 1994](#)). This simple log-quadratic fit for stars with mass between $0.6 M_{\odot}$ and $120 M_{\odot}$ (well encompassing the range of masses for SN progenitors) is given by equation 4.

Equation 4 gives stellar lifetimes in years, as a function of their metallicity Z and their mass M .

$$\begin{aligned} \log(t_*) &= a_0(Z) + a_1(Z) \log\left(\frac{M}{M_{\odot}}\right) + a_2(Z) \log^2\left(\frac{M}{M_{\odot}}\right), \\ a_0 &= 10.13 + 0.07547 \log(Z) - 0.008084 \log^2(Z), \\ a_1 &= -4.424 - 0.7939 \log(Z) - 0.1187 \log^2(Z), \\ a_2 &= 1.262 + 0.3385 \log(Z) + 0.05417 \log^2(Z) \end{aligned} \quad (4)$$

The stellar lifetimes are a strong function of their initial mass (as we might expect), but this fit does have some dependence on stellar metallicity (as is shown in [Figure 2](#)). We can simply invert this function and combine it with our IMF of choice to determine a SN rate as a function of time. SN progenitors are all massive enough that they fall in the Salpeter end of the IMF, with $\Phi(M) \propto M^{-1.3}$, for equations 1 and 2 resulting in a SN rate dN_{SN}/dt given by

$$\log \frac{dN_{\text{SN}}}{dt} = \log A + 1.3 \frac{a_1 + \sqrt{a_1^2 - 4a_2(a_0 - \log t)}}{2a_2} \quad (5)$$

Despite this form, the actual rate for reasonable masses ($\sim 5 - 100 M_{\odot}$) of SN progenitors is relatively constant, with the first SN detonating at $\sim 3 - 5$ Myr, and the final SN detonating at $\sim 30 - 70$ Myr.

A number of simulation codes and projects have used these rates directly to stochastically seed SNe (beginning with the original work of [Raiteri et al. 1996](#)), while others use the lifetimes to inform simpler models for the SN rates. An example of a fit to this relation (derived using [STARBURST99](#) ([Leitherer et al. 1999](#)) simulations) is the function used in the [FIRE](#) simulations for the

SN rate:

$$N_{\text{SN}}/M_{\odot} = \begin{cases} 0 & t_6 < 3.4 \\ (5.408t_6 - 18.39) \times 10^{-4} & 3.4 < t_6 < 10.37 \\ (2.516t_6 + 11.6) \times 10^{-4} & 10.37 < t_6 < 37.53 \\ 1.06 \times 10^{-2} & t_6 > 37.53 \end{cases} \quad (6)$$

N_{SN} is the cumulative number of SNe that a stellar population produces, divided by the initial mass of that population. The total energy released by a population of stars will simply be the product of the energy released per SN, e_{SN} and the number of SNe $E_{\text{SN}} = e_{\text{SN}} N_{\text{SN}}$. This can then be normalized by the population mass M_* , giving a total specific SN energy $\mathcal{E}_{\text{SN}} = E_{\text{SN}}/M_*$.

It is also a common approach to simply detonate all SNe simultaneously, either at the time of the first SN $t_0 \sim 3$ Myr, roughly the median SN time $t_0 \sim 15$ Myr, or at the time of the last SN $t_0 \sim 30$ Myr. As the total SN number (energy) budget is nearly linear in time, it is also a common approach to inject SN energy at a constant rate. A brief sampling of total specific SN energies \mathcal{E}_{SN} , SN start times t_0 , and durations τ_{SN} are given in [Table 1](#). This is in no way a comprehensive survey of every input rate that has been used to date, but is an example of what is commonly used, and what is used by recent and frequently cited simulations. Many of these models are also used in multiple works – for example, the [EAGLE](#) feedback models are also used in [APOSTLE](#) ([Sawala et al. 2016](#)) and [E-MOSAICS](#) ([Pfeffer et al. 2018](#); [Kruijssen et al. 2019a](#)) simulations. As these numbers show, there is both a wide variety in the energy budget for SNe as well as the timescales over which this energy is deposited. Instantaneous and continuous injection of energy are common approaches, while some simulations use fits to the IMF and the stellar lifetime function to produce more accurate, if more complex, SN injection rate functions.

3 METHODS

We run the simulations presented here in the moving-mesh semi-Lagrangian code [AREPO](#) ([Springel 2010](#)). [AREPO](#) uses an on-the-fly Voronoi tessellation to generate a mesh which follows the flow of fluid in a simulation and allows the use of optimally diffusive Riemann solvers in a Godunov-type scheme, while preserving Galilean invariance and allowing for automatic Lagrangian refinement. [AREPO](#) has been widely used to study galaxy formation in both large-volume cosmological simulations ([Vogelsberger et al. 2014](#)), cosmological zooms of individual galaxies ([Grand et al. 2017](#)), down to isolated galaxy simulations ([Smith et al. 2018](#)). We have added to [AREPO](#) the [GRACKLE 3.1](#) ([Smith et al. 2017](#)) non-equilibrium cooling library, which allows us to include primordial & metal line cooling using tabulated [CLOUDY](#) ([Ferland et al. 2013](#)) rates. In this study, we assume collisional ionization equilibrium and an initial ISM metallicity of $Z = 0.012$. We also include a non-thermal pressure floor to ensure that the [Truelove et al. \(1997\)](#) criterion is fulfilled and that artificial numerical fragmentation is suppressed when the Jeans length falls below the cell size.

Star formation is handled in this study using a simple [Schmidt \(1959\)](#) law prescription ([Katz 1992](#)). Stars are allowed to form in gas which has density exceeding 10 cm^{-3} , and with temperature below 10^4 K. Gas cells which satisfy this criterion then form stars stochastically, with a probability given by the SFR

$$\dot{\rho}_* = \epsilon_{\text{ff}} \rho / t_{\text{ff}} \quad (7)$$

In a given timestep, the probability of a gas cell forming a star is thus

$$P_{\text{SF}}(\delta t) = 1 - \exp\left(-\frac{\epsilon_{\text{ff}}\delta t}{t_{\text{ff}}}\right) \quad (8)$$

We use an efficiency per free fall time of $\epsilon_{\text{ff}} = 0.05$, appropriate within molecular clouds (e.g. [Evans et al. 2009](#)). After this probability is calculated, we draw a random number from a uniform distribution $[0, 1)$. If the probability P_{SF} exceeds this random number, the cell is fully converted to a star particle. As we use a Lagrangian refinement that ensures gas cells never vary by more than a factor of 2 from our target mass resolution of $8.59 \times 10^5 M_{\odot}$, this also ensures the star particles spawned in our simulation stay close to this target mass as well. While there are more complex models for star formation, the interplay of these models and stellar feedback is beyond the scope of this study.

As simply dumping thermal energy into gas will result in catastrophic overcooling when the Sedov radius of an individual SN is unresolved, we make use of a mechanical feedback model that has been demonstrated to produce converged momentum injection across many orders of magnitude in gas resolution ([Kimm & Cen 2014](#); [Hopkins et al. 2018a](#)). In brief, we determine the host cell of a star particle depositing feedback, and then use the Voronoi mesh around this cell to deposit momentum in the shell of the feedback bubble. For each cell which shares a face with the feedback-hosting cell, we calculate the area of that face $w_i = A_{ij}$, and use that to weight the momentum contribution for each cell. As AREPO provides both face areas and normals, we are able to ensure momentum conservation trivially. We use the terminal momentum at the end of the pressure-driven snowplow phase, following [Kimm & Cen \(2014\)](#), using the equations derived from high resolution one- and two-dimensional simulations of SN blasts:

$$p_{\text{term}} = 3 \times 10^5 \text{ km s}^{-1} M_{\odot} \max[Z/Z_{\odot}, 0.01]^{-0.14} E_{51}^{16/17} n^{-2/17} \quad (9)$$

For each cell surrounding the central one, we use the energy $E_i = w_i E$ and density to calculate p_{term} , and inject the minimum of the ejecta momentum or the terminal momentum:

$$p_{ij} = \min[\sqrt{2m_j w_i E}, w_i p_{\text{term}}] \quad (10)$$

This is essentially the same scheme used in [Hopkins et al. \(2018a\)](#) and [Smith et al. \(2018\)](#), but with one significant difference. In those methods, the remaining feedback energy after momentum injection is deposited into the same cells which receive momentum. We instead collect this thermal energy and deposit it into the central cell, effectively giving us a separation between the cold, swept up shell (which carries most of the momentum), and the hot, diffuse centre (which contains most of the thermal energy). We have determined that this results in little difference in the overall evolution of SN driven bubbles in isolation, as well as on the overall evolution of galaxies simulated with this feedback model compared to simply injecting both thermal and kinetic energy into the same cells. What it provides is the ability for more sophisticated treatments of marginally-resolved SN bubbles, which we will present in a future study.

We use the initial conditions (ICs) developed as part of the AGORA comparison project ([Kim et al. 2014](#)). This IC was designed to roughly match the Milky Way: it has a disc scale length of 3.43 kpc, and a scale height a tenth of this value. It is embedded in a dark matter (DM) halo with a mass $M_{200} = 1.07 \times 10^{12} M_{\odot}$ and virial radius $R_{200} = 205$ kpc. The halo concentration parameter is $c = 10$, and the [Bullock et al. \(2001\)](#) spin parameter is $\lambda = 0.04$.

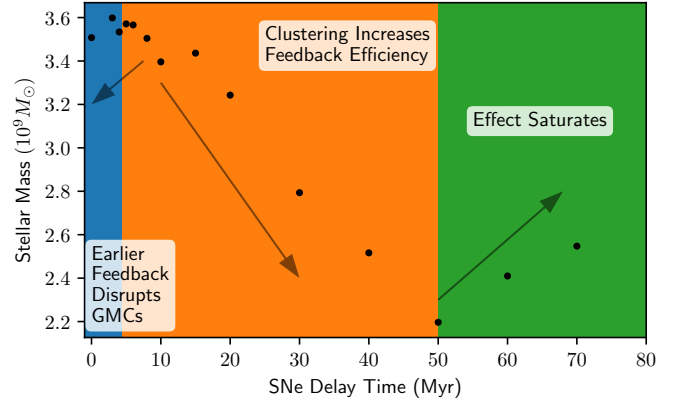


Figure 3. Stellar mass formed over 600 Myr as a function of SN delay time, shown as black points. We can see three regions (indicated here with different colors) where the relation between the total stellar mass and the delay time changes. We indicate three different regimes here. In blue, shorter delays reduce the SFR by disrupting star forming clouds before they reach high star formation efficiencies. In orange, we see the regime where increased clustering increases the efficiency of SN feedback. Finally, in the green region, we see this effect saturate, as stars formed co-spatially drift apart.

The IC contains a stellar disc and bulge, with a bulge to stellar disc ratio of 0.125, and a gas fraction of 0.18. The AGORA isolated disc ICs were generated using the MAKENEWDISK code described in [Springel et al. \(2005\)](#). We use a gravitational softening length of 80 pc, and a gas cell mass of $8.59 \times 10^4 M_{\odot}$. The IC star particle mass is $3.437 \times 10^5 M_{\odot}$, and the live DM halo contains 10^5 particles of mass $1.254 \times 10^7 M_{\odot}$ each. We initialize the gas in the simulation with a temperature of 10^4 K, though this is rapidly replaced with the equilibrium temperature determined by the ISM density and the [Haardt & Madau \(2012\)](#) UV background.

4 DOES IT MATTER WHEN SUPERNOVAE OCCUR?

In this section, we examine how the evolution of an isolated disc galaxy changes when the timing of SNe is changed while keeping the total SN energy budget constant. We will examine both instantaneous injection, where $\tau_{\text{SN}} = 0$, and continuous injection, where $\tau_{\text{SN}} > 0$. In each case, the total mass loss due to SNe is set to 10 per cent of the star particle’s initial mass, and the energy budget is set by this initial mass with the specific SN energy of $\mathcal{E}_{\text{SN}} = 10^{49} \text{ erg}/M_{\odot}$, corresponding to an energy released per SN of 10^{51} erg with $N_{\text{SN}} = 0.01 M_{\odot}^{-1}$.

4.1 Instantaneous injection and the SN delay time

Here we examine the results of dumping the entire SN energy budget instantaneously, after some delay time. As we previously showed in [Table 1](#), instantaneous SN injection is frequently used in many simulations that include SN feedback. In [Figure 3](#), we show the total stellar mass formed over the 600 Myr runtime of our simulations as a function of the delay time t_0 . As can be seen, there is a significant, nonlinear effect of the SN delay time on the averaged SFR/total stellar mass formed. For very short delays < 5 Myr (shown in blue), shorter delays can slightly reduce the star formation by disrupting star forming clouds before they have a chance to

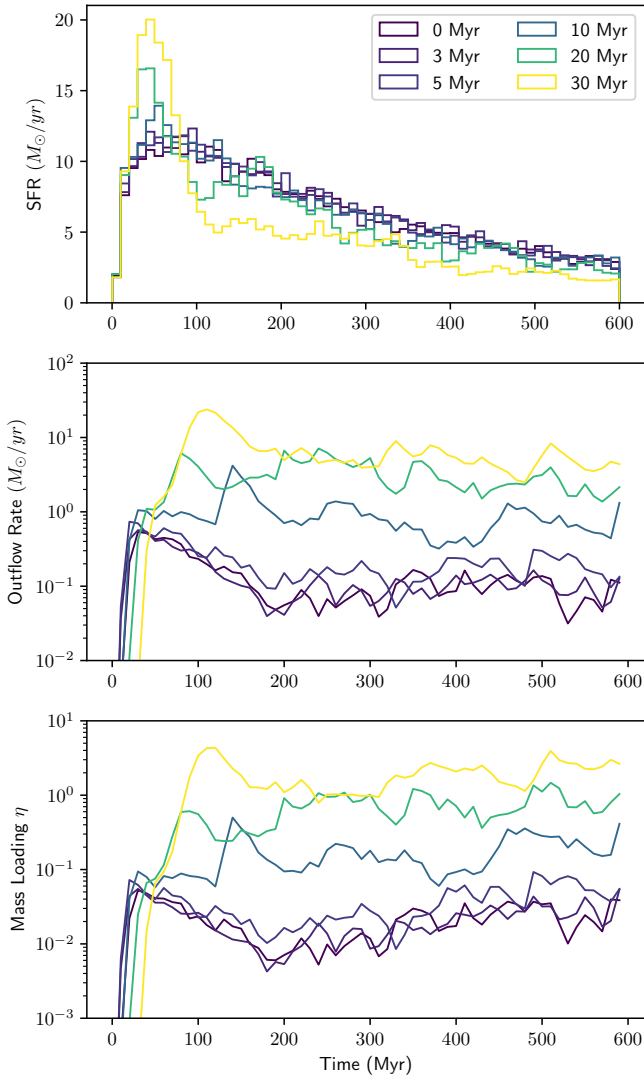


Figure 4. Star formation rates (top panel), outflow rates (centre panel), and mass loadings (bottom panel) for different SN delay times. The top panel shows that long SN delays ($t_0 = 20 - 30$ Myr) have clearly lower overall star formation rates, and that the intensity of the initial burst is larger for longer delays. As the middle and bottom panels show, the difference in outflow rates and mass loadings for $t_0 = 0 - 5$ Myr is negligible, while longer delay times result in significantly higher outflow rates and mass loadings, even long after the initial starburst has abated. Going from a delay of 5 Myr to 30 Myr reduces the average star formation rate for the final 400 Myr of the simulations by approximately one order of magnitude, but increases the mass loading by over two orders of magnitude.

fully collapse. For longer delay times, $\sim 5 - 50$ Myr, the star formation efficiency of individual clouds increases, resulting in much more clustered star formation, which subsequently drive stronger outflows. With delay times of $t_0 = 5 - 50$ Myr, there is significantly lower star formation with longer delay times, with a nearly 50% drop in stellar mass produced with $t_0 = 50$ Myr compared to $t_0 = 5$ Myr. Delays beyond this (> 50 Myr, shown in green) reverse the trend, as the local star formation efficiency in clouds has saturated at ~ 1 , and stars which were once more clustered drift apart. In order to verify the robustness of these results to run-to-run stochasticity, we re-simulate three of these delay times in

Appendix A, and show that the differences in SFR, outflow rates, and mass loadings are greater than run-to-run variance.

We show in Figure 4 how varying t_0 affects the evolution of three important quantities that are determined by the effectiveness SN feedback. In the top panel, we show the star formation rate, which shows how SN feedback is able to slow and regulate star formation. In the middle panel, we show the gas outflow rate (\dot{M}_{out}) from the galaxy, which shows how well SN feedback can drive galactic winds and fountains. Finally, we show in the bottom panel the mass loading ($\eta = \dot{M}_{out}/\text{SFR}$), the ratio of the two above quantities, which allows us to distinguish between outflows driven by efficient SN feedback from those driven by inefficient feedback, but high SFRs.

The reduced SFRs with long ($t_0 \geq 10$ Myr) delays is not uniform across the 600 Myr evolution of the galaxy. The top panel of Figure 4 shows that long delays produce a strong burst of star formation at the beginning of the simulation, as clouds are able to form and rapidly form stars without any regulation from SN feedback. This leads to a significant burst in star formation in the first 100 Myr, followed by a significant reduction in the overall SFR for the remaining time. We verify, in Appendix B, that this burst is not the source of the difference between simulations with different values of t_0 . In the centre panel of the same figure, we see that this burst in star formation is associated with a corresponding burst in gas outflowing from the galaxy. We calculate these outflow rates by taking all gas moving away from the disc within two planar slabs of thickness 500 pc located at 5 kpc above and below the disc. The outflow rate is then calculated, as in Keller et al. (2014), as the total momentum of outflowing gas in these slabs, divided by their thickness. After the initial starburst, the outflow rate is higher for longer delay times, with delays of 10 – 30 Myr giving comparable outflow rates of $\dot{M}_{out} \sim 1 - 10 M_{\odot} \text{yr}^{-1}$, and shorter delays producing outflow rates of $\dot{M}_{out} \sim 0.1 M_{\odot} \text{yr}^{-1}$. If we look at the mass loading η , we can see that there is a monotonic increase in mass loading with increased t_0 . This means that longer SN delay times will result in SN feedback that more effectively drives galactic winds, *without any changes to the SN energetics or numerical coupling algorithm*. The effect is especially striking when we compare the shortest delay (0 Myr) to the longest (30 Myr), with average mass loadings of $\eta = 0.021$ and $\eta = 1.7$ respectively, an increase of nearly two orders of magnitude.

The increased effectiveness of feedback at driving outflows is qualitatively striking when we look at gas column density maps for different SN delay times in Figure 5. The stronger outflows we saw previously for long delay times begin to significantly alter the disc morphology for delays of $t_0 \geq 10$ Myr. We see that the ISM becomes noticeably depleted, with nearly all gas being isolated to dense clumps and clouds along spiral arms, as the flocculent inter-cloud material is evacuated. Overall, we see much less dense ISM gas in the disc of galaxies with longer values of t_0 .

The reason for the increased effectiveness of SN feedback is the way that the SN delay time t_0 changes the clustering of star formation, which we can quantify with the stellar two point correlation function. As we show in Figure 6, the two point correlation function of stars recently formed (within the last 100 Myr) in the disc has significantly more clustered star particles with separations of < 300 pc when we increase t_0 beyond 10 Myr. We calculate the two point correlation function $\xi_2(r)$ using the Landy & Szalay (1993) estimator¹ with uncertainties calculated with 10 bootstrap

¹ The two point correlation function $\xi_2(r)$ is a measure of the excess prob-

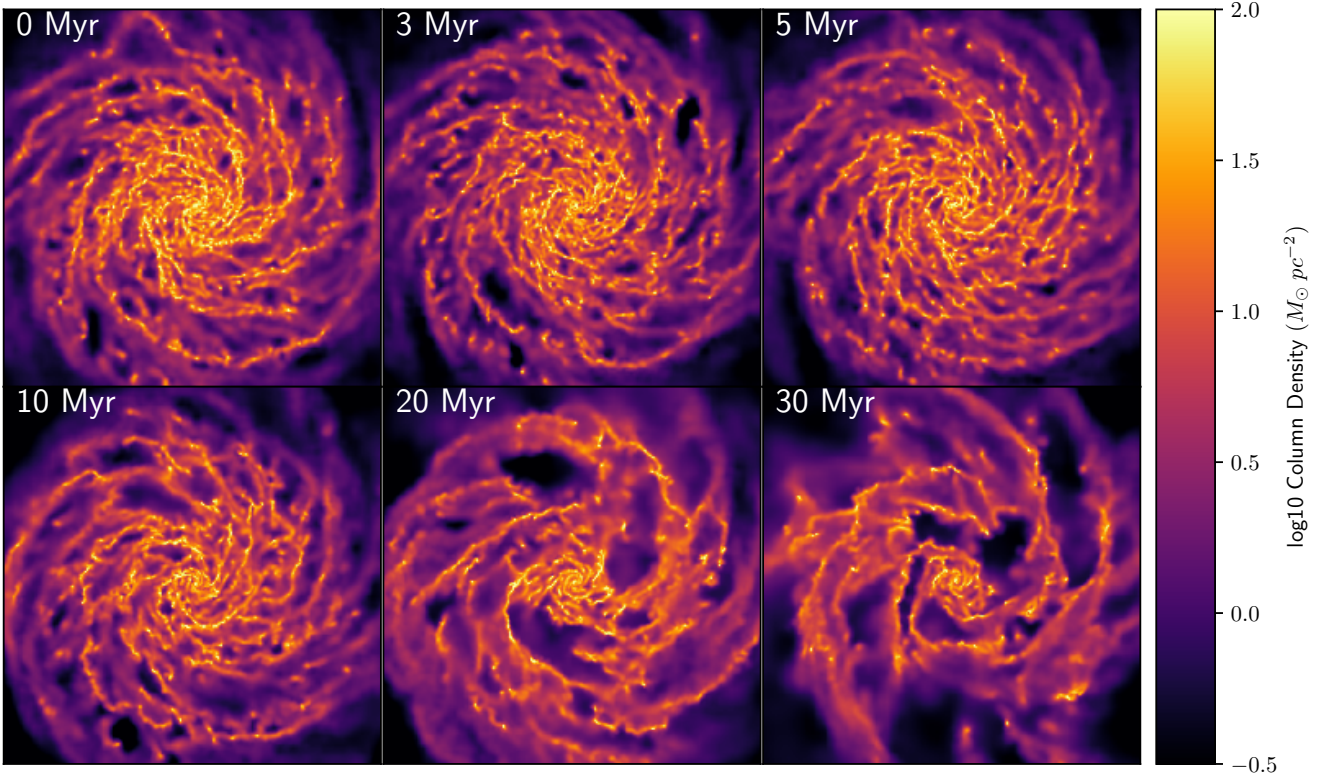


Figure 5. 30 kpc wide gas column density maps for different SN delay times. As can be seen here, longer delay times result in a much “emptier” ISM, with efficient outflows removing a large fraction of the gas from the disc. Much of the remaining mass is concentrated in a small number of dense clouds.

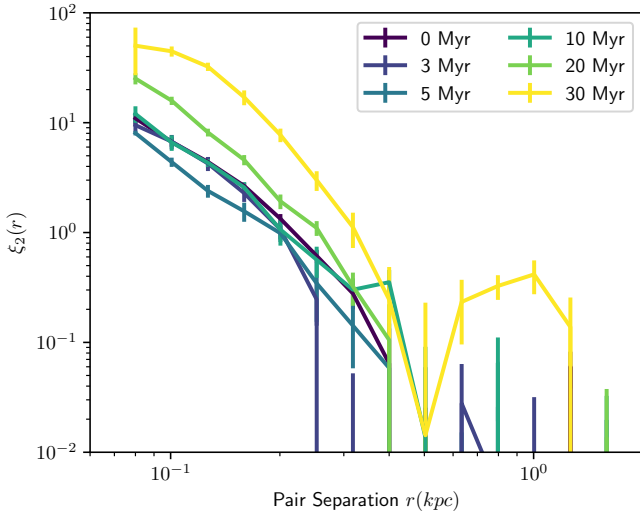


Figure 6. Two point correlation function $\xi_2(r)$ for young star particles (with ages < 100 Myr) in our simulations as a function of the SN delay time t_0 . For long delay times ($t_0 > 10$ Myr), clustering on < 200 pc length scales becomes significantly more likely than in the galaxies with shorter delay times.

ability of finding two stars within a separation of r against a random dis-

tribution. In order to exclude any structures “baked in” from the initial star burst and the symmetry of the initial conditions, we only look at stars formed in the final 100 Myr of the simulations. This also allows us to look specifically at stars that have not experienced significant migration away from the stars they are born along side. For delay times of $t_0 \geq 10$ Myr, we see little difference in $\xi_2(r)$, which matches the small changes we see in the SFR, galactic outflow rate, and ISM morphology shown in Figure 4 and Figure 5 (although the two point correlation function for $t_0 = 10$ Myr shows only marginally greater clustering than the runs with $t_0 < 10$ Myr, within the bootstrapped uncertainties of $\xi_2(r)$). The much greater probability of forming stars in clusters with long values of t_0 is simply a result of whether feedback is able to disrupt the star formation of a local region before simple gas exhaustion or galactic dynamics do so (Krujissen 2012). With short delay times, star forming regions form only a fraction of the available gas into stars, while long delay times allow star forming regions to reach their maximum integrated star formation efficiencies. A possible alternative explanation for the increased feedback efficiency with long delay times may be the ISM density in which SNe detonate. At low density, radiative cooling losses are reduced, and so feedback may couple

tribution. The Landy & Szalay (1993) estimator uses the number of actual pairs within a separation r , $DD(r)$, together with the number of random pairs given the same mean density $RR(r)$ and the cross-correlated data-random pairs $DR(r)$ to calculate $\xi_2(r) = (DD(r) - 2DR(r) + RR(r))/RR(r)$. As we are dealing with star particles distributed in a thin disc, the Landy & Szalay (1993) estimator is ideal, as it minimizes the errors occurring from a non-periodic distribution of points.

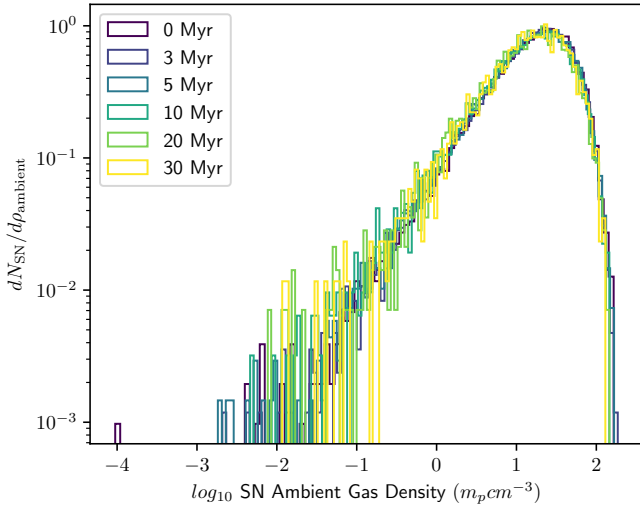


Figure 7. Local ISM density of SN events, as a function of the SN delay time. As can be seen here, there is no significant change in the ambient density of the ISM where SNe detonate when the SN delay time is changed. This implies that the increased feedback efficiency is not due to stars migrating out of dense regions before SNe, or gas being consumed by star formation before SNe occur.

more efficiently with the ISM. If long delay times allow more star forming gas to be consumed, or for stars to migrate out of their birth environments, they may detonate as SNe in significantly lower density gas. However, as Figure 7 shows, there is no significant change in the density of gas in which SNe detonate as a function of t_0 . If we restrict this to only examine stars formed in the last 100 Myr, as we do in the correlation functions, the distribution shows little change. This strongly suggests that it is the clustering, not the ambient ISM density, that increases the efficiency of instantaneously injected feedback with long delay times.

4.2 Instantaneous vs. continuous injection of energy

While the instantaneous injection of SN energy is a common technique in galaxy simulations, it is of course less physically motivated than using a realistic distribution of stellar initial masses and lifetimes, which together can produce an SN injection rate, as we derived in Section 2. We can reasonably approximate the injection rate for a Salpeter-like IMF and stellar lifetime function as a piecewise constant luminosity if the IMF in each stellar particle is fully sampled, and the number of SNe produced per star particle is more than ~ 10 (Mac Low & McCray 1988). As our stellar particle mass is $\sim 10^5 M_\odot$, this approximation holds comfortably. With a continuous injection of energy, we add a second timing parameter to the SN feedback, the duration of energy injection τ_{SN} . Here we probe within the range of “reasonable” physical uncertainty for t_0 and τ_{SN} . We simulate a grid of 6 galaxies, with delay times t_0 of 0 Myr, 3 Myr, and 5 Myr to approximate “early feedback” (as is done in Semenov et al. 2018), rapid SN onset, and slow SN onset respectively. We choose two durations times, 30 Myr and 40 Myr, that span the range of durations that have been commonly used in the literature.

Figure 8 shows that for similar delay times to instantaneous injection, continuous injection of SN energy produces roughly comparable star formation rates and higher, burstier outflow rates and

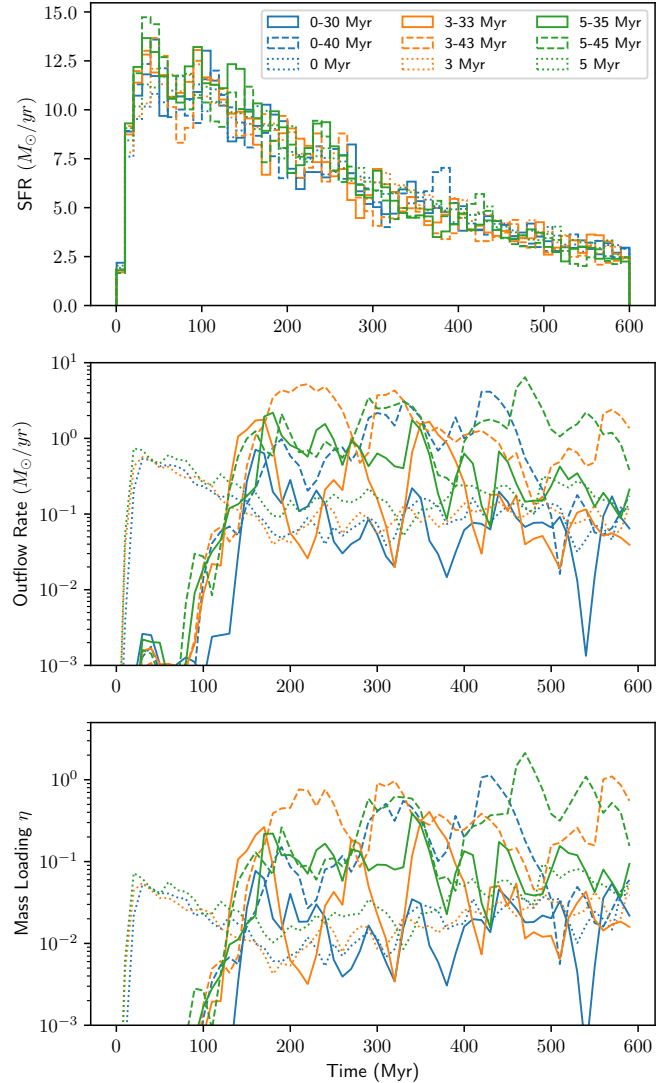


Figure 8. Star formation rates (top panel), outflow rates (centre panel), and mass loadings (bottom panel) for continuous SN injection with different delay times t_0 and durations τ_{SN} . Solid lines show results using a duration of $\tau_{\text{SN}} = 30$ Myr, while dashed lines show $\tau_{\text{SN}} = 40$ Myr. Dotted lines show the results for the same delay times with instantaneous injection. Blue, orange, and green curves show delay times of 0 Myr, 3 Myr, and 5 Myr respectively. Longer delay times result in a slightly lower SFR, with little discernible difference in outflow rates.

mass loadings, once the disk settles to a steady state. As with instantaneous injection, there is little difference in either star formation or outflow properties for changes in delay times of 0 – 5 Myr, and we see that there is no noticeable change in the SFR for SN durations of 40 Myr as opposed to 30 Myr. Generally, there are higher outflow rates and mass loadings for runs with longer durations ($\tau_{\text{SN}} = 0$ has lower average mass loadings for all runs with $\tau_{\text{SN}} > 0$, with the exception of the 0 – 30 Myr case). The average mass loadings for the three values of t_0 we examine here are $\eta = 0.026$ with $\tau_{\text{SN}} = 0$, $\eta = 0.05$ with $\tau_{\text{SN}} = 30$ Myr, and $\eta = 0.25$ for $\tau_{\text{SN}} = 40$ Myr. However, the galactic outflows in these galaxies are delayed in their launching from the initial starburst, peaking at 100 – 200 Myr, rather than in the first 50 Myr when $\tau_{\text{SN}} = 0$.

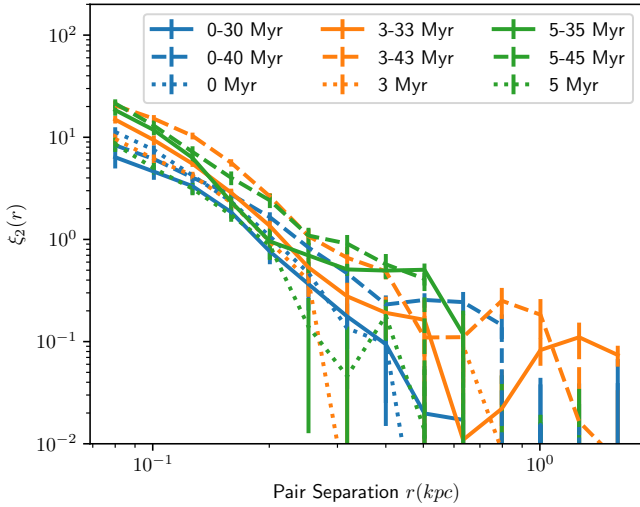


Figure 9. Two point correlation function $\xi_2(r)$ for star particles in our simulations as a function of the SN delay time t_0 and injection timescale τ_{SN} . As in Figure 8, solid lines show $\tau_{\text{SN}} = 30$ Myr, dashed lines show $\tau_{\text{SN}} = 40$ Myr, while dotted lines show instantaneous injection with the same delay time t_0 .

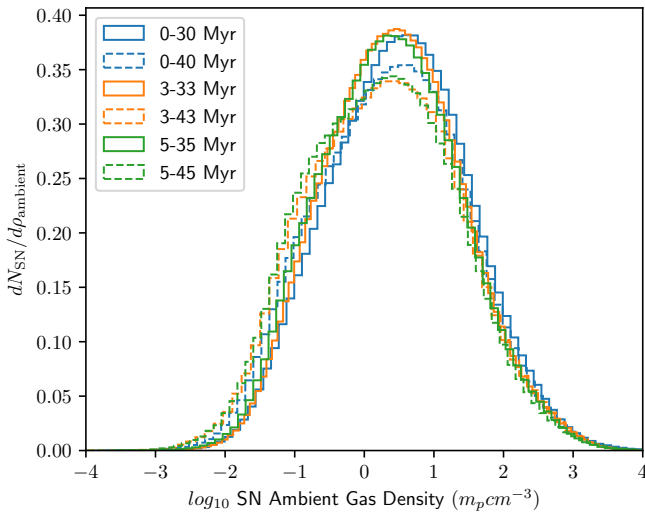


Figure 10. Local ISM density of SN events with continuous injection of SN energy (for comparison to instantaneous injection, see Figure 7). As can be seen, the typical densities of SN detonations during continuous injection are lower than those seen with instantaneous injection, with roughly log-normal distribution of ambient ISM densities as well. With longer (40 Myr) injection durations, we see a somewhat broader distribution of ambient densities, with a lower median density as well.

Interestingly, if we look at the same two point correlation function of star particles as we did for the instantaneous case, seen here in Figure 9, we see that the continuous injection of SN energy does not significantly change clustering on scales < 100 pc compared to instantaneous injection (though we do see that the case with the lowest outflow mass loading, 0–30 Myr also shows the lowest clustering of star formation). Continuous energy injection does, however, produce noticeable changes in the ambient density that SNe

explode in. As Figure 10 shows, the ambient density surrounding SN events is approximately log-normal, with lower mean densities than are seen for instantaneous injection. With instantaneous injection of SN energy, we see ambient ISM densities about SN events of $15 - 17 \text{ cm}^{-3}$. With continuous injection, longer durations produce lower ambient densities. For $\tau_{\text{SN}} = 30$ Myr we see ambient densities of 3.2 cm^{-3} , 2.7 cm^{-3} , and 2.4 cm^{-3} with $t_0 = 0, 3, 5$ Myr respectively. For $\tau_{\text{SN}} = 40$ Myr, we see ambient densities of 2.4 cm^{-3} , 1.9 cm^{-3} , and 1.7 cm^{-3} with $t_0 = 0, 3, 5$ Myr respectively.

Given these results, we naturally might ask why the significantly lower ambient SN densities seen for SN injected continuously (a factor of 2-5 times lower than for SN injected instantaneously) do not result in significantly higher outflow mass loadings? If the primary physical mechanism which sets the efficiency of outflow driving is radiative cooling in the ISM, we should see much higher mass loadings for the simulations which show lower ambient SN gas density. As we show in the summary Figure 11, the highest averaged mass loadings for SN injection with $t_0 = 0 - 5$ Myr and $\tau_{\text{SN}} = 0 - 40$ Myr do correspond to the lowest average densities. However, we do not see a sharp change in mass loadings going from instantaneous to continuous injection of SN energy that corresponds to the sharp change in ambient SN gas densities shown in the right hand panel of Figure 11. If the decrease in ambient density was combined with a corresponding decrease in stellar clustering, this might explain the relatively weak increase in outflow mass loadings we see. We also do not see a sharp change in the average number of young (< 100 Myr) stars within one scale height (343 pc) of every star particle as we move from instantaneous to continuous star formation. A different mechanism than the clustering of young stars is thus needed to explain the relatively small increase mass loadings we see for continuous injection of energy relative to instantaneous injection.

If we consider the evolution of a pressure-driven snowplow (for instantaneous injection) versus a wind (for continuous injection), we can see a possible solution to this question. Outflows will vent from the ISM once a superbubble radius reaches a scale height $r \sim h$. In both cases, a swept-up shell will rapidly form, with radiative cooling removing most of the thermal energy from this shell. For instantaneous injection, this shell will evolve with the familiar pressure-driven snowplow solution derived by McKee & Ostriker (1977). In this case, the radius of the bubble (from equation 9 and 12 in McKee & Ostriker 1977) will be given by the driving energy (E_{51} , in units of 10^{51} erg), the ambient density (n_0 , in units of cm^{-3}), and the time (t , in units of years):

$$r = 10^{0.33} E_{51}^{0.15} \left(\frac{t^2}{n_0} \right)^{1/7} \text{ pc.} \quad (11)$$

Setting this $r = h$ (in pc) to solve for the breakout time gives:

$$t_{\text{b,inst}} = 10^{-7.16} E_{51}^{-0.53} n_0^{1/2} h_{\text{pc}}^{7/2} \text{ Myr.} \quad (12)$$

We can then differentiate equation (11) and substitute $t_{\text{b,inst}}$ for t to solve for the breakout velocity:

$$v_{\text{b,inst}} = 10^{6.82} E_{51}^{0.53} n_0^{-1/2} h_{\text{pc}}^{-5/2} \text{ km s}^{-1}. \quad (13)$$

For a star cluster driving an energy conserving wind we can apply the classic Weaver et al. (1977) solution for the bubble radius:

$$r = 10^{-1.77} L_{38}^{1/5} t^{3/5} n_0^{-1/5} \text{ pc} \quad (14)$$

with a mechanical luminosity $L_{38} = (E/\tau_{\text{SN}})/10^{38} \text{ erg s}^{-1}$. To solve for the shell velocity, we first set $r_{\text{b}} = h$ (in pc) and invert

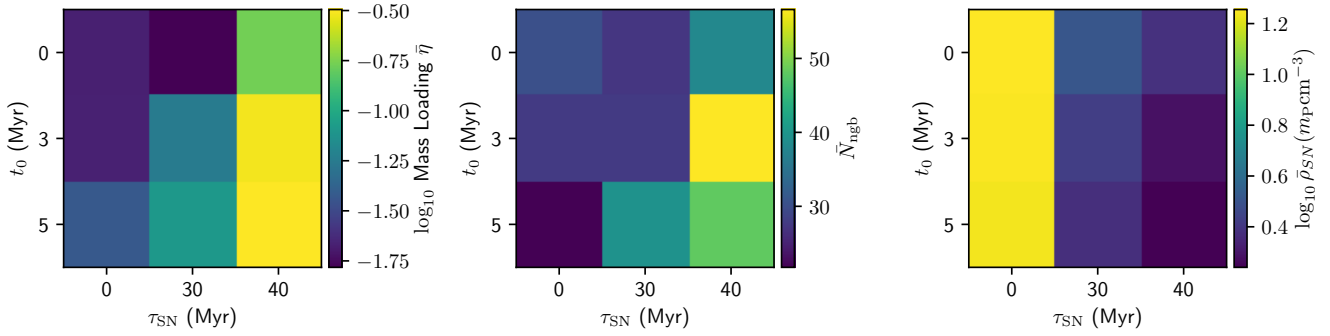


Figure 11. Summary of the average outflow mass loading (left panel), average number of young stellar neighbours per star particle (middle panel), and ambient SN density (right panel) for simulations with SN delay times of $t_0 = 0 - 5$ Myr and injection durations $\tau_{\text{SN}} = 0 - 40$ Myr. As can be seen here, mass loadings increase towards larger values of t_0 and τ_{SN} . A similar trend is seen in the ambient gas density surrounding SN events (though this trend is stronger for continuous SN energy injection. We also see a rough trend towards more clustered young star particles following this same trend.)

equation (14) to solve for t :

$$t_{\text{b,cont}} = 10^{-3.04} L_{38}^{-1/3} n_0^{1/3} h_{\text{pc}}^{5/3} \text{ Myr}. \quad (15)$$

By then differentiating equation (14) and substituting in $t = t_{\text{b,cont}}$ we find the velocity of a continuously-driven blastwave at the time of breakout is

$$v_{\text{b,cont}} = 10^{2.81} L_{38}^{1/3} n_0^{-1/3} h_{\text{pc}}^{2/3} \text{ km s}^{-1}. \quad (16)$$

For a single star particle with mass $8.9 \times 10^4 M_{\odot}$ (and thus $E = 8.9 \times 10^{53}$ erg), in an ISM with ambient density 15 cm^{-3} and a scale height of 343 pc, the velocity of a bubble at breakout for instantaneous injection of energy is $v_{\text{b,inst}} = 28 \text{ km s}^{-1}$, which occurs at $t_{\text{b,inst}} = 5.5$ Myr. For the same star particle, injecting its SN energy over $\tau_{\text{SN}} = 30$ Myr into an ambient density of 2 cm^{-3} , this breakout is instead $v_{\text{b,cont}} = 22 \text{ km s}^{-1}$, and occurs at $t_{\text{b,cont}} = 9.1$ Myr. If the mass loading of the galactic winds are primarily set by the velocity at breakout, this explains why the larger ambient densities seen for instantaneous injection of SN energy does not result in a significant reduction of the outflow mass loadings compared to the continuous injection of SN energy. Naturally, this one-dimensional analysis omits the stratification of gas within the galaxy, as bubbles will become hourglass-shaped as their radius becomes comparable to the gas scale height (Mac Low & McCray 1988), but is illustrative of how bubbles driven by an instantaneous blastwave evolve relative to those driven by a constant mechanical luminosity.

Despite the small differences in the average local density of SN injection and the clustering of stars for different values of τ_{SN} , we see higher outflow rates for galaxies simulated with longer ($\tau_{\text{SN}} = 40$ Myr) compared to shorter ($\tau_{\text{SN}} = 30$ Myr) injection durations. The previous analytic argument predicts that bubbles should break out of the ISM before the end of τ_{SN} . If this is the case, then SN occurring after the breakout occurs will be able to accelerate gas out of the disc unimpeded by the weight of the ISM above or below them. In Figure 12, we examine how the gas surface density surrounding young stars is altered by the injection of SN. This figure shows the evolution of the gas surface density within a circular patch with radius equal to the initial gas scale height $r = h = 343$ pc around each star particle for 50 Myr after formation. To probe the stars most likely to launch strong outflows, we calculate the lower 25th percentile of these profiles. The surface densities for all cases begin at $\sim 40 M_{\odot} \text{ pc}^{-2}$, and are reduced to $< 10 M_{\odot} \text{ pc}^{-2}$ by 50 Myr. As can be seen, however, more gas is

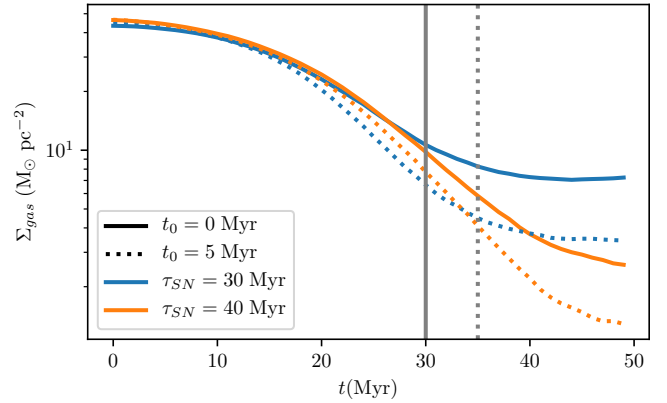


Figure 12. Gas surface density within a scale height of newly-formed star particles for their first 50 Myr with continuous injection of SN. We show the lower 25th percentile surface density to highlight the quarter of stars which are most able to drive outflows efficiently. Blue curves show the surface density evolution for $\tau_{\text{SN}} = 30$ Myr, while orange curves show the results for $\tau_{\text{SN}} = 40$ Myr. Solid curves show $t_0 = 0$ Myr, and dotted curves show $t_0 = 5$ Myr. The horizontal grey lines indicate the shut off point for $\tau_{\text{SN}} = 30$ Myr. Stars continuously reduce the gas surface density in their neighbourhood until the termination of feedback. With longer injection durations, this results in lower final surface densities 50 Myr after a star particle has formed. Only after the shut off of SN do the $\tau_{\text{SN}} = 30$ Myr and $\tau_{\text{SN}} = 40$ Myr cases begin to diverge significantly.

removed from the regions surrounding stars when $\tau_{\text{SN}} = 40$ Myr than when $\tau_{\text{SN}} = 30$ Myr, with surface densities ~ 4 times lower by 50 Myr. This difference does not begin until the termination of SN in the $\tau_{\text{SN}} = 30$ Myr case, suggesting that the size of SN-driven bubbles (and/or the ejection of outflows) depends weakly on τ_{SN} prior to the shut off of SN (as the relatively weak dependence on L_{38} in equation 14 would predict). If these bubbles do indeed break out before τ_{SN} , then the energy and momentum injected by SN will be able to vent directly into the halo. A larger fraction of the SN energy budget will be expended in this regime when τ_{SN} is longer, resulting in larger outflow mass loadings. This phenomenon is analogous to the “Powered Break-out” versus “Coasting Break-out” regime that was recently explored in (Orr et al. 2021), with

longer values of τ_{SN} spending longer in the ‘‘Powered Break-out’’ regime. Further study (such as high resolution simulations of instantaneous and continuous energy injection in a turbulent, fractal ISM) can potentially explain the nonlinear connection between the injection timescales of SN, radiative cooling losses, correlated star formation, and the breakout of superbubbles to drive galaxy-scale outflows.

In the next section, we show how the longer durations driven by changes in the minimum SN progenitor mass have an even stronger effect on the ambient density in which SNe detonate. This in turn drives even larger changes in the outflow rates than those we see here, due also in part to changes in the total SN energy budget. We also do not see any trend in the smallest-scale (< 100 pc) clustering between the two feedback durations we simulate, though in the intermediate (100 – 400 pc) scale, longer delays do appear to produce slightly more power in the two point correlation function. We leave a detailed study of how feedback shapes the clustering of star formation on the smallest (unresolved in these simulations) scales for future, higher resolution simulation work.

5 THE CRITICAL IMPORTANCE OF THE MINIMUM PROGENITOR MASS

In the previous sections, we have examined how purely numerical choices for approximating or simplifying the injection timescale of SN energy impact the effectiveness of the SN feedback at driving galactic outflows and regulating star formation. In each of these tests, we have assumed a constant specific SN energy produced per unit mass of stars formed, $\mathcal{E}_{SN} = 10^{49}$ erg M_{\odot}^{-1} , while varying only the SN delay time t_0 and injection timescale τ_{SN} . If we consider instead the observational and theoretical uncertainties in the minimum progenitor mass for SNe, as we have briefly described in Section 2, it is clear that a different minimum progenitor mass will change both τ_{SN} and \mathcal{E}_{SN} . To that end, we have run a set of 5 galaxies with SN energies and injection timescales corresponding to the values for a Chabrier (2003) IMF and a linear approximation of the Raiteri et al. (1996) stellar lifetimes for minimum progenitor masses of 6 – 10 M_{\odot} . The energies and timescales of these runs are listed in Table 2. The first SN is determined by the most massive progenitor, which we fix to 100 M_{\odot} in all runs, giving $t_0 = 3.3$ Myr. With a constant SN energy of 10^{51} erg, the minimum SN progenitor mass will strongly impact the total SN energy budget (\mathcal{E}_{SN}) by changing the number of SN produced per unit stellar mass formed (N_{SN}). Because we approximate the SN rate as constant (while in reality, roughly half of SNe occur in the first ~ 25 Myr even for the smallest realistic minimum progenitor mass), assuming a constant luminosity means that the luminosity for smaller progenitor masses will be slightly lower than for larger ones: with a 6 M_{\odot} minimum progenitor, the specific mechanical luminosity due to SNe is 7.46×10^{33} erg $s^{-1} M_{\odot}^{-1}$, while a 10 M_{\odot} minimum progenitor mass gives a specific luminosity of 1.08×10^{34} erg $s^{-1} M_{\odot}^{-1}$. While the instantaneous luminosity may be lower for a smaller progenitor mass, the longer time over which SNe detonate produce a larger integrated SN energy budget. Uncertainties in the minimum SN progenitor mass produce a much larger difference in the SN energy budget than uncertainties in the maximum SN progenitor mass or the form of the IMF, as we showed in figure 1. While uncertainties in the evolution of SN remnants and the radiative losses that may occur in an unresolved, magnetized, turbulent ISM are most likely larger than the $\mathcal{O}(2)$ difference that the choice of minimum progenitor produces, all models

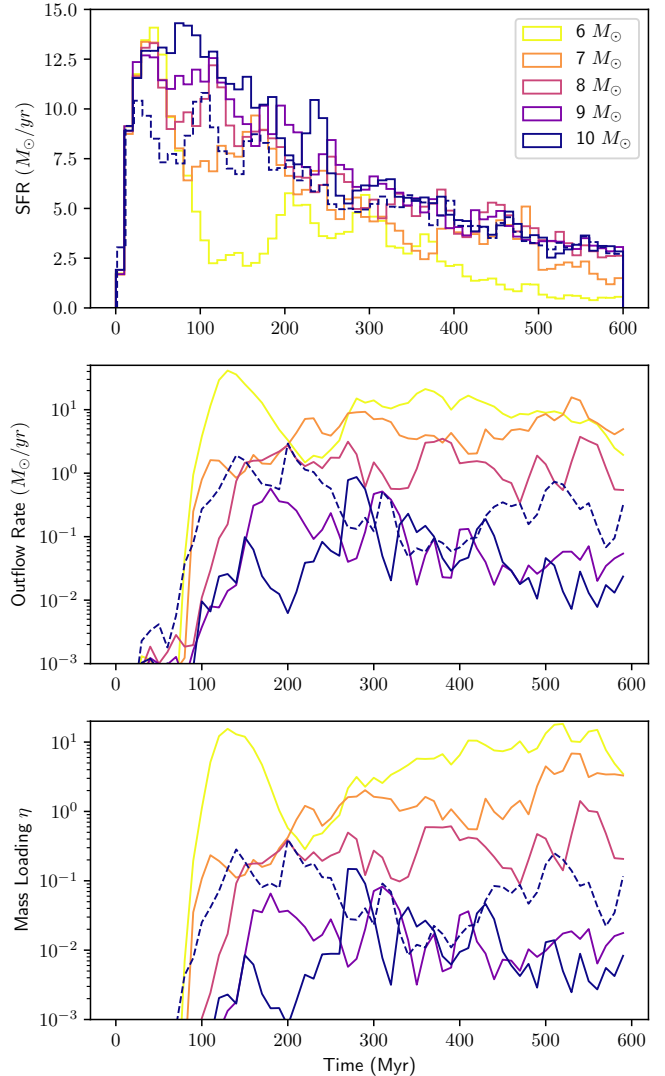


Figure 13. Star formation rates (top panel), outflow rates (centre panel), and mass loadings (bottom panel) for continuous SN injection with different minimum SN progenitor masses. All solid curves show the results with the feedback energy and duration for a given minimum SN progenitor mass (see table 2). The single dashed curve shows the a simulation with the energy budget of a 6 M_{\odot} minimum progenitor mass, but with the shorter duration of a 10 M_{\odot} minimum progenitor mass. As the top panel shows, the larger SN budget and longer duration of SN feedback greatly reduces the overall star formation rate when lower minimum SN progenitor masses are used. This results in a corresponding increase in the outflow mass loading, as fewer stars are able to drive comparable amounts of material out of the galactic disc.

for capturing these effects must begin with an energy budget set by the range of masses for SN progenitors.

The star formation and outflow mass loadings for these different progenitor masses can be seen in Figure 13. We see here that (as we might expect), the ~ 2 times higher SN energy budget and ~ 3 times longer injection duration between the smallest progenitor mass (6 M_{\odot}) and the largest progenitor mass (10 M_{\odot}) result in a larger reduction in the SFRs compared to changing the timescale of feedback alone, as we examined in the previous section. With a 6 M_{\odot} minimum progenitor mass, star formation in the

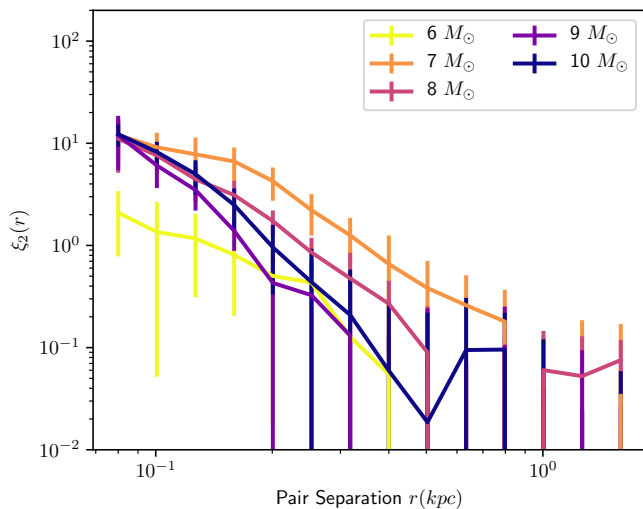


Figure 14. Two point correlation function $\xi_2(r)$ for star particles in our simulations as a function of the minimum SN progenitor mass. Unlike the cases with longer SN delay times, we see here that the reduced SFR and increased outflow mass loading are not due to increased stellar clustering, but simply due to the higher SN energy budget along with a change in the ambient ISM density SNe detonate in.

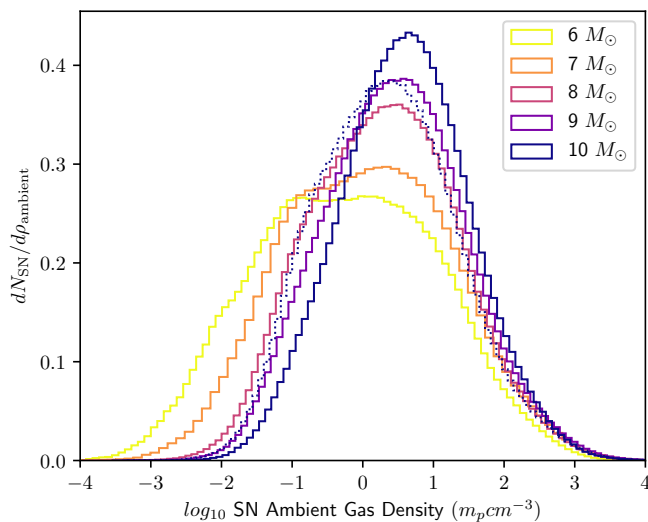


Figure 15. Local ISM density of SN events, as a function of the minimum SN progenitor mass. Unlike what we see for single SN events with various delay times in Figure 7, varying the minimum progenitor mass has a noticeable change in the typical density in which SNe detonate. Longer injection durations produce a broader distribution of ambient gas densities surrounding SN events, with a reduction in the mean density. As in Figure 13, we show in the dashed curve a case where the energy budget of a $6 M_\odot$ minimum SN mass is combined with the injection duration of a $10 M_\odot$ minimum progenitor mass. When this larger energy budget is given a shorter injection duration, we see that the ambient density about SNe increases.

Minimum Progenitor Mass	\mathcal{E}_{SN} (erg/ M_\odot)	τ_{SN} (Myr)
$6 M_\odot$	1.6×10^{49}	68
$7 M_\odot$	1.3×10^{49}	48
$8 M_\odot$	1.1×10^{49}	37
$9 M_\odot$	9.4×10^{48}	29
$10 M_\odot$	8.2×10^{48}	24

Table 2. Specific feedback energy \mathcal{E}_{SN} and feedback duration for different minimum SN progenitor masses derived with a maximum mass of $100 M_\odot$ and the IMF and stellar lifetimes given by equations 2 and 4. Increasing the minimum progenitor mass from $6 M_\odot$ to $10 M_\odot$ not only decreases the overall SN energy budget by a factor of ~ 2 , it also decreases the duration of SN injection by a factor of ~ 3 .

disc is noticeably reduced, with winds driven to an average mass loading of $\eta = 5.5$, more than 2 orders of magnitude larger than the average mass loading for a $10 M_\odot$, with $\eta = 0.015$. The dashed curve in Figure 13 shows the result of combining the energy budget of a $6 M_\odot$ minimum progenitor mass (1.6×10^{49} erg/ M_\odot) with the injection duration of a $10 M_\odot$ minimum SN progenitor mass (24 Myr). As this figure shows, the effects of changing the progenitor mass arise from *both* the increased energy budget and longer SN duration. As we saw previously in figure 8, the continuous injection of FB energy can drive stronger outflows compared to instantaneous injection. Reducing the injection duration by roughly a third, from 68 Myr to 24 Myr, reduces the effectiveness of SN feedback at regulating star formation and driving outflows (although less than if we were to also reduce the feedback energy to 8.2×10^{48} erg/ M_\odot).

If we look at the two point correlation function (Figure 14), we see again that unlike with instantaneous injection of SN energy, the increased effectiveness of SN-driven outflows for small minimum progenitor masses is not associated with an increase in the clustering of star formation. Instead, these results point to the much simpler effect of higher SN energy budgets and longer SN injection timescales (resulting in less cooling losses compared to an instantaneous injection) produce a much stronger driving engine for powering galactic outflows. The reduction in cooling losses are clearly revealed if we examine the ambient ISM densities in which SNe detonate in Figure 15. Here we see the continuous injection of SNe over 24 – 68 Myr results in a roughly log-normal distribution, without the slight skewness seen in Figure 7. In general, we see two major trends: the width of the distribution of SN events grows with lower minimum progenitor mass, and the median of the distribution decreases. For instantaneous injection of energy, the mean ambient ISM density SN events detonate in is $15 - 17 \text{ cm}^{-3}$ (for values of t_0 from 0 – 30 Myr), while we see mean ambient ISM densities for SN events of 0.6 cm^{-3} , 1.2 cm^{-3} , 2.0 cm^{-3} , 2.8 cm^{-3} , and 3.9 cm^{-3} for minimum progenitor masses of $6 M_\odot$, $7 M_\odot$, $8 M_\odot$, $9 M_\odot$, and $10 M_\odot$ respectively. Together with the broader distribution of ambient densities, this results in 30% of all SN energy being deposited in gas with ambient density below 0.1 cm^{-3} with a $6 M_\odot$ minimum progenitor mass, compared to only 4% for a $10 M_\odot$ progenitor. As has been shown in past work (Sharma et al. 2014; Genety et al. 2017), SNe detonating in the low-density remnants of past SNe suffer less cooling losses and convert more energy into kinetic motions than SNe detonating in “pristine”, gas rich environments.

As the dashed curve in Figure 15 shows, the higher SN energy budget of a $6 M_\odot$ minimum progenitor mass (1.6×10^{49} erg/ M_\odot), combined with the shorter SN duration of a $10 M_\odot$ minimum pro-

genitor (24 Myr vs. 68 Myr) does not give the broad, lower-density distribution we see from setting both the energy budget and duration to the $6 M_{\odot}$ values, but instead is closer to the results of the short-duration injection from a $9 - 10 M_{\odot}$ minimum progenitor mass. This explains why the outflow and star formation rates shown in Figure 13 does not show as significant change when the energy budget alone is increased (shown in the dashed curve in that figure as well). The importance of the progenitor comes not only from the change in SN energy budget, but in the duration of injection as well. A longer duration allows the most massive SN progenitors, which detonate early, to pre-process the ISM prior to the detonation of the least massive SN progenitors. This effect mimics early feedback, which has been shown to significantly increase the effectiveness of SN feedback (Stinson et al. 2013; Hopkins et al. 2014).

6 DISCUSSION

We have seen that the choice of SN delay time t_0 and duration τ_{SN} in simple models for the SN injection rate can have noticeable effects on the ability of SN feedback at regulating star formation and significant effects on their effectiveness at driving outflows. When SNe are injected instantaneously, with an entire stellar population’s SN budget deposited at once, choosing a delay time t_0 of 0 Myr vs. 30 Myr can change the average SFR by nearly 50%, and the outflow mass loadings by nearly two orders of magnitude, by greatly increasing the clustering of star formation. It has been shown that clustered SNe lose less energy to cooling (Sharma et al. 2014; Walch & Naab 2015), produce higher terminal momenta (Gentry et al. 2017), and ultimately drive more powerful outflows (Fielding et al. 2018). Fielding et al. (2017) examined the effect of clustering directly using idealized, high resolution simulations of isolated dwarf galaxies. By keeping the SN rate constant, but varying the fraction of SNe which occur co-spatially (the clustering fraction f_{cl}), they showed that the mass loading of winds is related to the clustering fraction $\eta \propto f_{\text{cl}}^{1.05}$ (also see Sect. 7.3.4 of Kruijssen 2012). The results we have shown here reveal that the SN injection rate can change the spatial clustering of star formation, resulting in a similar effect to this. Clustering has been explicitly employed in the stochastic feedback model of Dalla Vecchia & Schaye (2012), which artificially increases the clustering of feedback to overcome numerical losses. It has also been seen to be a natural consequence of self-gravity (Martizzi 2020), where the increased clustering seen in the two-point correlation of star particles has been directly tied to more effective SN driven galactic outflows. Clustering of star formation has been used in similar simulations to these as a tool to compare simulations to observations and constrain parameters in models for feedback and star formation (Buck et al. 2019). As we show in Table 1, instantaneous injection of SNe is a popular approximation, and delay times from 0 – 30 Myr have been used in a number of simulations of cosmological and isolated galaxy evolution. Our results suggest that these choices can have comparable effect size to the choice of sub-grid model for SN feedback.

With a more realistic model for the SN delay time distribution, giving a continuous injection of energy rather than a simple instantaneous one, we find that the sensitivity to SN delay time t_0 and duration τ_{SN} is less clear. We do not see a significant change in the star formation rate the past the initial starburst, although we do see somewhat higher averaged outflow mass loadings with longer delay times. Interestingly, the most notable change is a decrease in the “smoothness” of the outflows (when $\tau_{\text{SN}} > 0$), with order-of-magnitude variations occurring over ~ 100 Myr periods.

This suggests that a more realistic model of SN energy injection may shift towards a stronger “fountain” mode of galactic outflows, where gas is ejected but later re-accreted. In Gentry et al. (2020), the authors found that instantaneous injection of FB energy significantly reduced the overall momentum injection, but it is important to consider that the mechanism there (and the mechanism in Fielding et al. (2018)) may be different than what we show here, as we do not resolve the cooling radius of most SNe. Thus, any changes in the cooling processes on small-scales are not captured by our simulations.

Unfortunately, not all uncertainty can be removed simply by avoiding the instantaneous injection simplification. Our results in Section 5 show that, using a realistic SN delay time distribution designed to fit a Chabrier (2003) IMF and a Raiteri et al. (1996) stellar lifetime function, there is still a major uncertainty in the SN distribution model. The minimum SN progenitor mass, as the review by Smartt (2009) details, is uncertain by at least $1 M_{\odot}$. This means that both the overall SN energy budget, as well as the SN injection duration, are both uncertain to within roughly $\sim 50\%$. As Figure 13 shows, this has a noticeable effect on the overall SFR of the galaxy and the ability of feedback to drive outflows.

An interesting result we have seen as well is the difference in sensitivity to feedback parameters between the SFR and outflow properties. Changing the delay time t_0 results in a relatively small ($\sim 50\%$) change in SFR, yet drives a change of nearly two orders of magnitude in outflow rates and mass loadings. This suggests that the strongest observational tests of SN feedback will be in examinations of the circumgalactic medium (CGM) and the metal budget of galaxies. The CGM is where outflows deposit themselves, and we are now beginning to see comprehensive observational studies of their mass budgets and kinematics (Werk et al. 2014; Prochaska et al. 2017), which is helping to inform new models for outflows, the CGM, and galaxy evolution (Voit et al. 2019; Keller et al. 2020). In particular, the strong changes in mass loadings suggest that surveys of the metal loss budget (Kirby et al. 2011; Peebles et al. 2014; Telford et al. 2019) will be a powerful tool for constraining the detailed parameters of stellar feedback.

We have explored here the impact of three related parameters that must be chosen for any model of SN feedback: the delay between star formation and the first SN (t_0), the duration over which SNe detonate (τ_{SN}), and the total SN energy budget \mathcal{E}_{SN} . These parameters may be chosen as simplified numerical approximations of the SN delay-time distribution and energetics, or as a more physically motivated function of the IMF, stellar lifetimes, and SN progenitor mass function. This is, however, only a fraction of the potential sources of uncertainty in the impact of SN feedback.

Of course, SNe are not the only form of stellar feedback, and stellar feedback is not the only feedback that may influence the evolution of a galaxy. Energy released from accretion onto supermassive black holes can power active galactic nuclei (AGN) which heat the galaxy (McNamara & Nulsen 2007) and drive fast outflows (Morganti et al. 2003). However, AGN activity occurs in galactic nuclei, spatially decoupled from the local star forming regions, and will only change the temporal and spatial clustering of star formation on the scale of the galaxy itself. Other forms of feedback from massive stars, however, will have a similar effect to the parameters we have manipulated here. Stellar winds (e.g. Gatto et al. 2017), expanding HII regions (e.g. Franco et al. 1990), ionizing radiation (e.g. Dale et al. 2005), and radiation pressure (e.g. Krumholz & Matzner 2009) will all act to change the total stellar feedback energy budget and SN coupling efficiency, as all of these processes begin immediately after star formation. These “early” feedback

mechanisms are likely responsible for the destruction of molecular clouds (Kruijssen et al. 2019b; Chevance et al. 2020, 2022; Kim et al. 2021). It has been shown in previous simulation studies (Agertz et al. 2013; Stinson et al. 2013; Hopkins et al. 2014) that the interaction of these multiple feedback mechanisms can result in a nonlinear change in the effectiveness of SN feedback, more than simply changing the overall energy budget. This is most easily explained through two channels: the pre-processing of ISM gas, lowering the density in which SNe detonate; and the termination of star formation in dense gas earlier than the 3 – 5 Myr delay required for the first SN. However, our results in Section 4.2 suggest that an earlier onset of feedback, without any additional energy or momentum, has a much smaller effect than the use of a realistic delay time distribution. How a more complete accounting of the feedback budget might change our results is a question we leave for future study.

In order to directly compare these universal parameters, rather than the details of the numerical coupling scheme, we have restricted our simulations to use a single sub-grid model for SN feedback, the Kimm & Cen (2014) mechanical feedback model that has been widely exploited in the literature. Previous studies have shown that choices related to the sub-grid model can have significant impact on the amount of numerical overcooling (Thacker & Couchman 2000), SFRs (Scannapieco et al. 2012), and outflow properties (Rosdahl et al. 2017). Choices such as which sub-grid model to use, what mass/length scale to deposit feedback over, and other model-specific parameters can change the behaviour of SN feedback to an extent comparable to (or even greater than) the changes in the model-independent parameters we have studied here. In particular, the changes in mass loadings seen when different sub-grid models were compared by Rosdahl et al. (2017) and Smith et al. (2018) are comparable in magnitude to the effect of changing t_0 from 5 Myr to 30 Myr with instantaneous injection of SN energy, or changing the minimum SN progenitor mass from $6 M_{\odot}$ to $10 M_{\odot}$. The most extreme changes in sub-grid model, however, can produce changes in the SFR significantly larger than we see here, with variations of nearly an order of magnitude. Unlike these purely numerical choices, however, the changes in the SN energy budget and duration that arise from different minimum progenitor masses are driven by uncertainties in the fundamental, underlying physics of stellar evolution and SNe detonation. Inferring the progenitor mass of a SN is a non-trivial process that involves assumptions both in the stellar evolution model (Williams et al. 2018) as well as the distribution of interstellar and circumstellar gas and dust (Kochanek et al. 2012). On top of that, SNe are relatively infrequent events, and only a few dozen events with identified progenitors have been observed (Smartt 2015). As long as the uncertainty in the minimum mass of SN progenitors is large, the energy budget of SN feedback will have significant uncertainties as well.

We have assumed here that the SN progenitor mass is a continuous range, with all stars between the minimum and maximum progenitor masses detonating as SNe. However, this simplifying assumption may not hold. SN progenitors with initial masses above $\sim 18 M_{\odot}$ have not been observed (Smartt 2015), suggesting that there may be mechanisms in core collapse that can prevent the escape of the potential energy that drives SNe. Simulations of SN core collapse have suggested that there exist “islands of explodability” where the density profile of the progenitor stellar core allows the neutrino-driven shock to prevent the fallback of the outer layers of the star. Stars outside this mass range may collapse directly to form a black hole without a detectable SN explosion (Horiuchi et al. 2014). The regions in which failed SNe occur may depend not

only on mass, but also on metallicity (Heger et al. 2003), rotation (Hirschi et al. 2004), and binarity (Eldridge et al. 2008). On top of this, whether a SN will fail to occur may not be a binary process, with regions producing SN fractions anywhere from 0 to 1 (Pejcha & Thompson 2015).

Finally, we have also assumed that all SNe detonate with the same energy, 10^{51} erg, independent of their mass or metallicity. Just as there may be regions of the stellar mass-metallicity plane where failed SNe occur, their may also be regions where sub-luminous or superluminous SNe occur. While type II-P SNe are the most common core collapse SN type (as these are the form that the lowest-mass progenitors are expected to take, Smartt 2009), other core collapse SNe may also be a significant component of the total SN budget. SNe associated with gamma ray bursts (GRBs) may release as much as 2×10^{54} erg (Woosley & Bloom 2006), and sub-luminous SNe have been observed with kinetic energies as low as $\sim 10^{47}$ erg (Lovegrove & Woosley 2013). While the most energetic GRBs are likely rare, sub-luminous SNe may be as significant a component of the massive star end sequence as are failed SNe. The “islands of explodability” that are currently the dominant observational and theoretical paradigm (Heger et al. 2003; Smartt 2009; Horiuchi et al. 2014) for massive star evolution do not all produce comparable energies, and the more massive stars may end their lives in hypernovae that produce 10-100 times as much energy as typical type II-P SN (Nomoto et al. 2011). An exploration of how a more physically motivated input sequence for SN feedback in galaxies that takes into account this more complex picture of SN energetics is an interesting possible future line of research.

7 CONCLUSION

We have shown here that a few parameters, key to all models for SN feedback in galaxy simulations, can have a significant impact on the evolution of a galaxy. A summary of our primary findings are as follows.

- Even if the total SN energy budget is kept constant, changing the delay between star formation and the first SN (t_0) or the duration of SNe (τ_{SN}) can have significant effects on the ability of SNe to regulate star formation and drive outflows.
- Long delays ($t_0 > 20$ Myr) between star formation and SN feedback can significantly increase the clustering of star formation, and thereby increase the effectiveness of SN feedback.
- The outflow rate and mass loading of galactic winds is a much more sensitive probe of SN feedback timing parameters t_0 and τ_{SN} than the overall star formation rate.
- Instantaneously injecting SN feedback at or near the time of first SN detonation does not significantly change the clustering of star formation or the overall star formation rate compared to injecting energy over time, but can reduce the outflow mass loadings of SN-driven winds relative to SNe injected over a realistic timescale (30 – 40 Myr).
- Continuous injection of SN energy can reduce the ambient ISM density SN energy is deposited into, increasing the efficiency of SN feedback at regulating star formation and driving outflows as the duration of injection increases.
- The observational and theoretical uncertainty in the minimum SN progenitor mass has a dramatic impact on both the timing and energy budget of SN feedback. Lowering the minimum SN progenitor mass reduces the star formation rate, and can increase outflow rates nearly 2 orders of magnitude.

- Lower minimum SN progenitor masses injects more SN energy over a longer duration. This of course increases the total feedback energy budget, but also results in a larger fraction of SN energy deposited in low-density ISM that has been pre-processed by the earliest SNe. This in turn dramatically reduces cooling losses, and increases how much kinetic energy each SN event deposits into the ISM.

What these results show is that choices in how to represent the SN rate function can have dramatic effects. These choices must be made regardless of the sub-grid method used to capture the effect of SN feedback, and can result in differences in the star formation and outflow evolution that is comparable to the differences produced when using different sub-grid models. Some of these choices are simple numerical simplifications, such as injecting all SNe instantaneously after a fixed delay time. The importance of the delay time choice can be eliminated by using a more realistic distribution for the SN lifetimes, giving a delay time distribution that spreads SNe over tens of Myr. However, even if we use a realistic delay time distribution for SNe, the current theoretical and observational uncertainties in the minimum mass SN progenitor translate into uncertainties in the SN injection duration and overall energy.

These uncertainties can also drive large changes in the evolution of the galaxy: changing the minimum SN progenitor mass from $7 M_{\odot}$ to $9 M_{\odot}$ results in a roughly $\sim 25\%$ increase in the overall star formation rate, and a nearly ten-fold reduction in the outflow mass loadings. These findings raise serious doubts as to the level of uncertainty we should have when interpreting the results of galaxy simulations. A well-developed literature has shown that the choice of SN sub-grid models can have dramatic impact on the evolution of the galaxy. We have shown here that there are choices below that sub-grid, in the injection timescales and SN budget, that can also dramatically impact the galaxy. There is clearly still significant uncertainty in the effectiveness of SN feedback at regulating star formation and driving outflows in galaxy simulations. Taking together our results, we recommend future simulations use at the least a constant injection of SN energy, rather than an instantaneous approximation. Along with this, whenever possible, simulations should bound their results by running examples with integrated SN energies and durations for minimum progenitor masses of $7 M_{\odot}$ and $9 M_{\odot}$: $\tau_{\text{SN}} = 48$ Myr with $\mathcal{E}_{\text{SN}} = 1.3 \times 10^{49}$ erg M_{\odot}^{-1} for a $7 M_{\odot}$ minimum progenitor, and $\tau_{\text{SN}} = 29$ Myr with $\mathcal{E}_{\text{SN}} = 9.4 \times 10^{48}$ erg M_{\odot}^{-1} for a $9 M_{\odot}$ minimum progenitor. While this will result in a modest increase in computational expense, it will allow one to quantify the impact that uncertainties in underlying SN physics have on all predictions made by these future simulations.

ACKNOWLEDGEMENTS

We thank Volker Springel for allowing us access to AREPO. The analysis was performed using `astroML` (<http://astroml.org>, Vanderplas et al. 2012) and `pynbody` (<http://pynbody.github.io/>, Pontzen et al. 2013). BWK acknowledges funding in the form of a Postdoctoral Research Fellowship from the Alexander von Humboldt Stiftung. BWK and JMDK gratefully acknowledge funding from the European Research Council (ERC) under the European Union's Horizon 2020 research and innovation programme via the ERC Starting Grant MUSTANG (grant agreement number 714907). JMDK gratefully acknowledges funding from the Deutsche Forschungsgemeinschaft (DFG, German Research Foundation) through an

Emmy Noether Research Group (grant number KR4801/1-1) and the DFG Sachbeihilfe (grant number KR4801/2-1).

DATA AVAILABILITY STATEMENT

The simulation data used in this paper will be shared on reasonable request to the corresponding author.

REFERENCES

- Agertz O., Kravtsov A. V., Leitner S. N., Gnedin N. Y., 2013, *ApJ*, **770**, 25
- Alongi M., Bertelli G., Bressan A., Chiosi C., Fagotto F., Greggio L., Nasi E., 1993, *A&AS*, **97**, 851
- Bastian N., Covey K. R., Meyer M. R., 2010, *ARAA*, **48**, 339
- Bertelli G., Bressan A., Chiosi C., Fagotto F., Nasi E., 1994, *A&AS*, **106**, 275
- Booth C. M., Agertz O., Kravtsov A. V., Gnedin N. Y., 2013, *ApJ*, **777**, L16
- Bressan A., Fagotto F., Bertelli G., Chiosi C., 1993, *A&AS*, **100**, 647
- Buck T., Dutton A. A., Macciò A. V., 2019, *MNRAS*, **486**, 1481
- Bullock J. S., Dekel A., Kolatt T. S., Kravtsov A. V., Klypin A. A., Porciani C., Primack J. R., 2001, *ApJ*, **555**, 240
- Ceverino D., Klypin A., Klimek E. S., Trujillo-Gomez S., Churchill C. W., Primack J., Dekel A., 2014, *MNRAS*, **442**, 1545
- Chabrier G., 2003, *PASP*, **115**, 763
- Chevance M., et al., 2020, *MNRAS*, **493**, 2872
- Chevance M., et al., 2022, *MNRAS*, **509**, 272
- Crain R. A., et al., 2015, *MNRAS*, **450**, 1937
- Dale J. E., Bonnell I. A., Clarke C. J., Bate M. R., 2005, *MNRAS*, **358**, 291
- Dalla Vecchia C., Schaye J., 2012, *MNRAS*, **426**, 140
- Dobbs C. L., Burkert A., Pringle J. E., 2011, *MNRAS*, **417**, 1318
- Dubois Y., Teyssier R., 2008, *A&A*, **477**, 79
- Dubois Y., Devriendt J., Slyz A., Teyssier R., 2012, *MNRAS*, **420**, 2662
- Ekström S., et al., 2012, *A&A*, **537**, A146
- Eldridge J. J., Izzard R. G., Tout C. A., 2008, *MNRAS*, **384**, 1109
- Evans Neal J. I., et al., 2009, *ApJS*, **181**, 321
- Ferland G. J., et al., 2013, *RMxAA*, **49**, 137
- Fielding D., Quataert E., Martizzi D., Faucher-Giguère C.-A., 2017, *MNRAS*, **470**, L39
- Fielding D., Quataert E., Martizzi D., 2018, *MNRAS*, **481**, 3325
- Franco J., Tenorio-Tagle G., Bodenheimer P., 1990, *ApJ*, **349**, 126
- Gatto A., et al., 2017, *MNRAS*, **466**, 1903
- Genel S., et al., 2019, *ApJ*, **871**, 21
- Gentry E. S., Krumholz M. R., Dekel A., Madau P., 2017, *MNRAS*, **465**, 2471
- Gentry E. S., Madau P., Krumholz M. R., 2020, *MNRAS*, **492**, 1243
- Gerritsen J. P. E., 1997, PhD thesis, Groningen University, the Netherlands, (1997)
- Girichidis P., et al., 2016, *ApJ*, **816**, L19
- Grand R. J. J., et al., 2017, *MNRAS*, **467**, 179
- Haardt F., Madau P., 2012, *ApJ*, **746**, 125
- Heger A., Fryer C. L., Woosley S. E., Langer N., Hartmann D. H., 2003, *ApJ*, **591**, 288
- Hirschi R., Meynet G., Maeder A., 2004, *A&A*, **425**, 649
- Hopkins P. F., Kereš D., Oñorbe J., Faucher-Giguère C.-A., Quataert E., Murray N., Bullock J. S., 2014, *MNRAS*, **445**, 581
- Hopkins P. F., et al., 2018a, *MNRAS*, **477**, 1578
- Hopkins P. F., et al., 2018b, *MNRAS*, **480**, 800
- Horiuchi S., Nakamura K., Takiwaki T., Kotake K., Tanaka M., 2014, *MNRAS*, **445**, L99
- Hu C.-Y., 2019, *MNRAS*, **483**, 3363
- Joung M. K. R., Mac Low M.-M., 2006, *ApJ*, **653**, 1266
- Jubelgas M., Springel V., Enßlin T., Pfrommer C., 2008, *A&A*, **481**, 33
- Katz N., 1992, *ApJ*, **391**, 502
- Kay S. T., Pearce F. R., Frenk C. S., Jenkins A., 2002, *MNRAS*, **330**, 113

- Keller B. W., Wadsley J., Benincasa S. M., Couchman H. M. P., 2014, *MNRAS*, **442**, 3013
- Keller B. W., Wadsley J., Couchman H. M. P., 2016, *MNRAS*, **463**, 1431
- Keller B. W., Wadsley J. W., Wang L., Kruijssen J. M. D., 2019, *MNRAS*, **482**, 2244
- Keller B. W., Kruijssen J. M. D., Wadsley J. W., 2020, *MNRAS*, **493**, 2149
- Kim J.-h., et al., 2014, *ApJS*, **210**, 14
- Kim J.-h., et al., 2016, *ApJ*, **833**, 202
- Kim J., et al., 2021, *MNRAS*, **504**, 487
- Kimm T., Cen R., 2014, *ApJ*, **788**, 121
- Kirby E. N., Martin C. L., Finlator K., 2011, *ApJ*, **742**, L25
- Kochanek C. S., Khan R., Dai X., 2012, *ApJ*, **759**, 20
- Kroupa P., 2001, *MNRAS*, **322**, 231
- Kruijssen J. M. D., 2012, *MNRAS*, **426**, 3008
- Kruijssen J. M. D., Pfeffer J. L., Crain R. A., Bastian N., 2019a, *MNRAS*, **486**, 3134
- Kruijssen J. M. D., et al., 2019b, *Nature*, **569**, 519
- Krumholz M. R., Matzner C. D., 2009, *ApJ*, **703**, 1352
- Landy S. D., Szalay A. S., 1993, *ApJ*, **412**, 64
- Larson R. B., 1974, *MNRAS*, **169**, 229
- Leitherer C., et al., 1999, *ApJS*, **123**, 3
- Leitherer C., Ekström S., Meynet G., Schaerer D., Agienko K. B., Levesque E. M., 2014, *ApJS*, **212**, 14
- Lovegrove E., Woosley S. E., 2013, *ApJ*, **769**, 109
- Mac Low M.-M., McCray R., 1988, *ApJ*, **324**, 776
- Martizzi D., 2020, *MNRAS*, **492**, 79
- McKee C. F., Ostriker J. P., 1977, *ApJ*, **218**, 148
- McNamara B. R., Nulsen P. E. J., 2007, *ARAA*, **45**, 117
- Morganti R., Oosterloo T. A., Emons B. H. C., van der Hulst J. M., Tadhunter C. N., 2003, *ApJ*, **593**, L69
- Navarro J. F., White S. D. M., 1993, *MNRAS*, **265**, 271
- Nomoto K., Maeda K., Tanaka M., Suzuki T., 2011, *Ap&SS*, **336**, 129
- Offner S. S. R., Clark P. C., Hennebelle P., Bastian N., Bate M. R., Hopkins P. F., Moraux E., Whitworth A. P., 2014, in Beuther H., Klessen R. S., Dullemond C. P., Henning T., eds, *Protostars and Planets VI*. p. 53 ([arXiv:1312.5326](https://arxiv.org/abs/1312.5326)), doi:10.2458/azu_uapress_9780816531240-ch003
- Orr M. E., Fielding D. B., Hayward C. C., Burkhardt B., 2021, arXiv e-prints, p. [arXiv:2109.14656](https://arxiv.org/abs/2109.14656)
- Peeples M. S., Werk J. K., Tumlinson J., Oppenheimer B. D., Prochaska J. X., Katz N., Weinberg D. H., 2014, *ApJ*, **786**, 54
- Peeples M. S., et al., 2019, *ApJ*, **873**, 129
- Pejcha O., Thompson T. A., 2015, *ApJ*, **801**, 90
- Pfeffer J., Kruijssen J. M. D., Crain R. A., Bastian N., 2018, *MNRAS*, **475**, 4309
- Pontzen A., Roškar R., Stinson G., Woods R., 2013, pynbody: N-Body/SPH analysis for python (ascl:1305.002)
- Prochaska J. X., et al., 2017, *ApJ*, **837**, 169
- Raiteri C. M., Villata M., Navarro J. F., 1996, *A&A*, **315**, 105
- Rogers H., Pittard J. M., 2013, *MNRAS*, **431**, 1337
- Rosdahl J., Schaye J., Dubois Y., Kimm T., Teyssier R., 2017, *MNRAS*, **466**, 11
- Salpeter E. E., 1955, *ApJ*, **121**, 161
- Sawala T., et al., 2016, *MNRAS*, **457**, 1931
- Scannapieco C., Tissera P. B., White S. D. M., Springel V., 2006, *MNRAS*, **371**, 1125
- Scannapieco C., et al., 2012, *MNRAS*, **423**, 1726
- Schmidt M., 1959, *ApJ*, **129**, 243
- Sedov L. I., 1959, *Similarity and Dimensional Methods in Mechanics*
- Semenov V. A., Kravtsov A. V., Gnedin N. Y., 2018, *ApJ*, **861**, 4
- Sharma P., Roy A., Nath B. B., Shchekinov Y., 2014, *MNRAS*, **443**, 3463
- Smartt S. J., 2009, *ARAA*, **47**, 63
- Smartt S. J., 2015, *Publ. Astron. Soc. Australia*, **32**, e016
- Smith B. D., et al., 2017, *MNRAS*, **466**, 2217
- Smith M. C., Sijacki D., Shen S., 2018, *MNRAS*, **478**, 302
- Springel V., 2010, *MNRAS*, **401**, 791
- Springel V., Hernquist L., 2003, *MNRAS*, **339**, 289
- Springel V., Di Matteo T., Hernquist L., 2005, *MNRAS*, **361**, 776
- Stinson G., Seth A., Katz N., Wadsley J., Governato F., Quinn T., 2006, *MNRAS*, **373**, 1074
- Stinson G. S., Brook C., Macciò A. V., Wadsley J., Quinn T. R., Couchman H. M. P., 2013, *MNRAS*, **428**, 129
- Taylor G., 1950, *Proceedings of the Royal Society of London Series A*, **201**, 159
- Telford O. G., Werk J. K., Dalcanton J. J., Williams B. F., 2019, *ApJ*, **877**, 120
- Teyssier R., 2002, *A&A*, **385**, 337
- Teyssier R., Pontzen A., Dubois Y., Read J. I., 2013, *MNRAS*, **429**, 3068
- Thacker R. J., Couchman H. M. P., 2000, *ApJ*, **545**, 728
- Truelove J. K., Klein R. I., McKee C. F., Holliman John H. I., Howell L. H., Greenough J. A., 1997, *ApJ*, **489**, L179
- Valentini M., Borgani S., Bressan A., Murante G., Tornatore L., Monaco P., 2019, *MNRAS*, **485**, 1384
- Vanderplas J., Connolly A., Ivezić Ž., Gray A., 2012, in *Conference on Intelligent Data Understanding (CIDU)*. pp 47 –54, doi:10.1109/CIDU.2012.6382200
- Vogelsberger M., et al., 2014, *MNRAS*, **444**, 1518
- Voit G. M., Donahue M., Zahedy F., Chen H.-W., Werk J., Bryan G. L., O’Shea B. W., 2019, *ApJ*, **879**, L1
- Walch S., Naab T., 2015, *MNRAS*, **451**, 2757
- Weaver R., McCray R., Castor J., Shapiro P., Moore R., 1977, *ApJ*, **218**, 377
- Werk J. K., et al., 2014, *ApJ*, **792**, 8
- Williams B. F., Hillis T. J., Murphy J. W., Gilbert K., Dalcanton J. J., Dolphin A. E., 2018, *ApJ*, **860**, 39
- Woosley S. E., Bloom J. S., 2006, *ARAA*, **44**, 507

APPENDIX A: ROBUSTNESS TO STOCHASTICITY

Recent studies (Keller et al. 2019; Genel et al. 2019) have shown that galaxy evolution shows non-trivial stochasticity, owing to the chaotic nature of the N-body problem that describes said evolution. Here we attempt to quantify this effect in our simulations, in order to ensure that our results are indeed due to the changes in clustered star formation and wind driving, rather than random run-to-run variations. In order to do this, we re-simulate 8 instances of our instantaneous SN injection cases with 0 Myr, 5 Myr, and 30 Myr delays. In order to seed variations between the 8 runs, we use a different number of cores for each, thus introducing differences in the domain decomposition and communication patterns at the level of floating-point roundoff.

As can be seen in Figure A1, the variation in star formation rates is large enough that the delays of 0 Myr and 5 Myr are nearly indistinguishable 300 Myr after the beginning of the run and the initial starburst. The drop in SFR for the longer delay, however, is significant enough that the difference is nearly always outside the run-to-run variation. For the outflow rates and mass loading, there is both a larger difference between the median values for each delay time, and a larger run-to-run variation. The differences between the delay times, though, are clearly evident, and we can therefore say with confidence that increased wind launching efficiency that occurs for longer SN delay times is a real effect, and not simply a fluke produced by random variance.

APPENDIX B: SENSITIVITY TO INITIAL STARBURST

Isolated galaxy simulations frequently suffer from transient bursts in star formation shortly after the simulation begins. We see this in the simulations presented here, and similar effects can be seen in the isolated galaxies from other studies (e.g. Keller et al. 2014, Rosdahl et al. 2017, Valentini et al. 2019). In order to verify that the

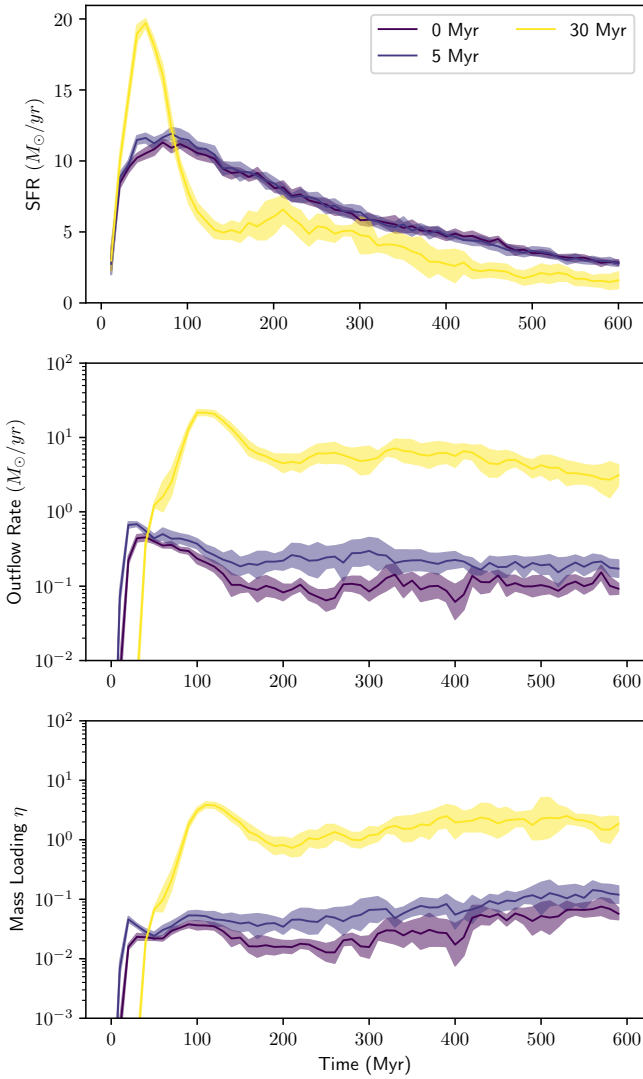


Figure A1. Median values (solid lines) and $\pm 1\sigma$ variance (shaded regions) for the star formation rate (top panel), mass outflow rate (middle panel), and outflow mass loading (bottom panel) for sets of 8 variance re-simulations with SN delay times of 0 Myr, 5 Myr, and 30 Myr. As can be seen, the difference in SFR between the two shorter delay times are mostly within the run-to-run uncertainty after 300 Myr, but the difference between these and the longer delay are distinct save for a short bursty period from 200 – 400 Myr. The outflow rates and mass loadings, however, are significantly different, even despite the larger variances for each case.

effects we see here are not simply due to the different strength of the initial starburst, we ran two additional experiments. In figure 4, it is clear that longer SN delays produce a stronger initial burst in star formation. Thus, it is possible that the changes in the star formation and outflow rates are a result of this initial burst re-shaping the disc ISM. To verify this is not the case, we took the two extremal simulations ($t_0 = 0$ Myr and $t_0 = 30$ Myr) and re-started them at the 300 Myr point with swapped values for t_0 . This gives us two additional runs to compare: a run which spends the first 300 Myr with $t_0 = 0$ Myr and the final 300 Myr with $t_0 = 30$ Myr, and a run which spends the first 300 Myr with $t_0 = 30$ Myr and the final 300 Myr with $t_0 = 0$ Myr.

If the strength of the initial burst in star formation is the cause

of the differences between the $t_0 = 0$ Myr and $t_0 = 30$ Myr runs we see in section 4.1, then changing the value of t_0 after this burst has completed shouldn't change the evolution of the galaxy. However, if the initial burst is not important, and the on-going star formation (and its clustering) is what establishes the changes we have seen, then changing the value of t_0 should push the SFR, outflow rates, and mass loadings towards the values they would have had if t_0 was set to the final value since the beginning of the simulation. In other words, changing the value of t_0 from 0 Myr to 30 Myr should slightly decrease the star formation rate and significantly increase the outflow rate, while doing the opposite change should produce the opposite result. As we show in figure B1, this is exactly what occurs. This demonstrates clearly that the effects we have examined are not simply the aftereffects of the initial burst in star formation.

We also verify that the initial burst of star formation as the disc settles is not dominating the changes we see in varying the minimum SN progenitor mass. As with the previous experiment, we compare simulations that use $6 M_\odot$ and $10 M_\odot$ minimum SN progenitor masses for their entire 600 Myr duration to runs that swap the minimum progenitor mass at 300 Myr. In figure B2, we show that the simulations which swap the minimum progenitor mass rapidly diverge from the simulations which do not. While they do not settle to the exactly same star formation and outflow rates, the simulations that swap the minimum mass behave similarly to the simulations which do not, but share the same final minimum SN progenitor mass. This again verifies that the difference we see in the star formation and outflow rates are not simply an artifact of the initial star burst.

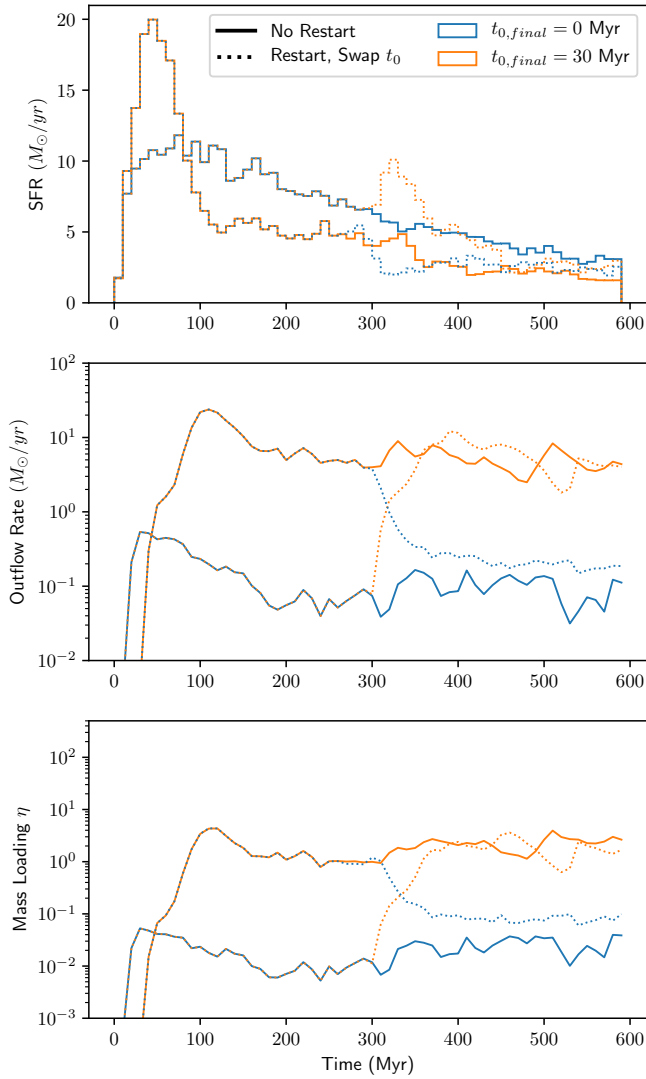


Figure B1. Comparison of the star formation rate (top panel), outflow rate (middle panel), and mass loading (bottom panel) of four permutations of the SN delay time t_0 . The two solid lines are run for all 600 Myr with constant t_0 , while the dashed lines swap the value of t_0 from 0 Myr to 30 Myr or vice versa at 300 Myr. As is clear, the final star formation rates, outflow rates, and mass loadings are set by the value of t_0 after the initial star burst, not the value during the star burst.

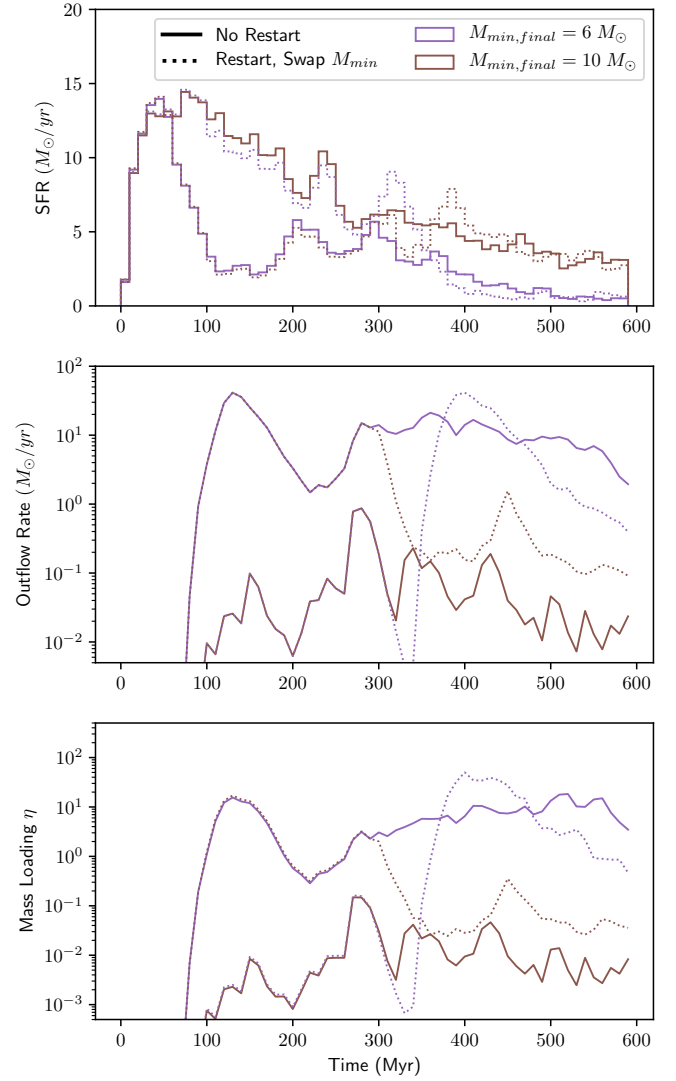


Figure B2. Comparison of the star formation rate (top panel), outflow rate (middle panel), and mass loading (bottom panel) of four permutations of the minimum SN progenitor mass M_{min} . The two solid lines are run for the entire simulation with constant minimum SN progenitor mass ($6 M_\odot$ in purple, $10 M_\odot$ in brown). The dashed lines swap the value of the minimum progenitor mass at 300 Myr. As this shows, the initial burst in star formation from the initial conditions does not set the differences we see in the star formation rates, outflow rates, and mass loadings. These differences are instead set by the change the strength of SN feedback for different progenitor masses.